HHS Public Access
Author manuscript
Dev Cell. Author manuscript; available in PMC 2024 November 06.

Wound-healing plasticity enables clonal expansion of founder progenitor cells in colitis

Cambrian Y. Liu[*,1,2], **Nandini Girish**[2,3], **Marie L. Gomez**[4], **Martin Kalski**[1], **Jessica K. Bernard**[5], **Benjamin D. Simons**[6,7,8], **D. Brent Polk**[*,2,3,9,10,+]

[1]Department of Medicine, The University of Chicago, Chicago, IL 60637 USA

[2]Division of Pediatric Gastroenterology, Hepatology, and Nutrition, Children's Hospital Los Angeles, Los Angeles, CA 90027 USA

[3]Department of Pediatrics, University of California San Diego School of Medicine, La Jolla, CA 92093 USA

[4]Program in Biomedical and Biological Sciences, Keck School of Medicine of the University of Southern California, Los Angeles, CA 90033 USA

[5]Program in Craniofacial Biology, Herman Ostrow School of Dentistry of the University of Southern California, Los Angeles, CA 90033 USA

[6]Wellcome Trust/Cancer Research UK Gurdon Institute, University of Cambridge, Cambridge CB2 1QN UK

[7]Department of Applied Mathematics and Theoretical Physics, Centre for Mathematical Sciences, University of Cambridge, Cambridge CB3 0WA UK

[8]Wellcome Trust/Medical Research Council Stem Cell Institute, University of Cambridge, Cambridge CB2 0AW UK

[9]Department of Biochemistry and Molecular Medicine, Keck School of Medicine of the University of Southern California, Los Angeles, CA 90033 USA

[10]Division of Pediatric Gastroenterology, Hepatology, and Nutrition, Rady Children's Hospital, San Diego, CA 92123 USA

Summary

Correspondence: C.Y.L. (cambrian@uchicago.edu), D.B.P. (dpolk@ucsd.edu). [*]Co-corresponding authors.
[+]Lead contact

Chronic colonic injury and inflammation pose high risks for field cancerization, wherein injury-associated mutations promote stem cell fitness and gradual clonal expansion. However, the long-term stability of some colitis-associated mutational fields could suggest alternate origins. Here, studies of acute murine colitis reveal a punctuated mechanism of massive, neutral clonal expansion during normal wound healing. Through 3d imaging, quantitative fate-mapping, and single-cell transcriptomics, we show that epithelial wound repair begins with the loss of structural constraints on regeneration, forming fused labyrinthine channels containing epithelial cells reprogrammed to a non-proliferative plastic state. A small but highly proliferative set of epithelial founder progenitor cells (FPCs) subsequently emerges and undergoes extensive cell division, enabling fluid-like lineage mixing and spreading across the colonic surface. Crypt budding restores the glandular organization, imprinting the pattern of clonal expansion. The emergence and functions of FPCs within a critical window of plasticity represent regenerative targets with implications for preneoplasia.

Graphical Abstract
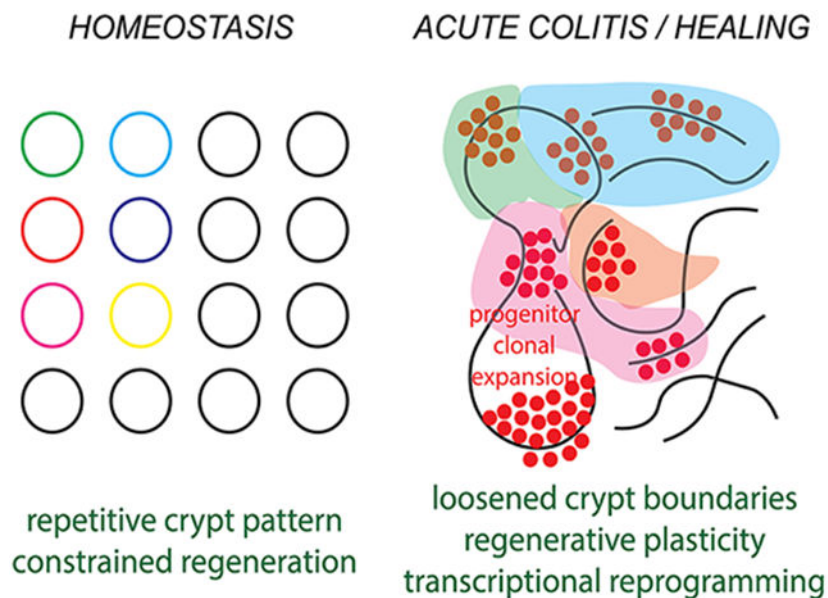
eTOC

Cancer is a common outcome of inflammatory bowel disease and may stem from repeated cycles of epithelial wounding and healing. Studying acute murine colitis and normal healing, Liu et al. detail the emergence and massive clonal expansion of a highly proliferative epithelial progenitor cell population within specialized wound-associated crypt structures.

Introduction

Long-term exposure to disease-associated tissue injury and inflammation increases the risks of dysplasia and cancer. An example of this occurs with inflammatory bowel disease (IBD), in which chronic ulceration and inflammation of the colon markedly increases colorectal cancer risk[1]. DNA damage from the injurious microenvironment can lead to mutagenesis:

if mutant epithelial stem cells acquire a fitness advantage, they may spread through the colon by seeding multiple crypts in a process of field cancerization[2,3]. Studies of directed mutagenesis in the uninjured murine intestinal epithelium support the lateral spread of fitness-advantaged stem cells and crypts through enhanced crypt fission and fusion rates[4-8]. However, the degree of mutant field expansion seems limited and does not easily explain the large clones seen in human tissue. Moreover, in many IBD patients, the large mutational fields observed in noncancerous tissue[9-14] often contain passenger mutations that confer no known fitness advantage[15], or even undergo extinction[16]. This raises the question of how these clones form, and whether there are other processes that can drive field change. At the same time, injury can drive a process of natural cellular reprogramming, leading to extensive remodeling of tissue during regeneration. Here we tested how injury and natural healing may drive enhanced clonal expansion, which could provide an alternative mechanism to drive field cancerization of mutant cells.

The disease course in IBD, as in other chronic inflammatory diseases, is characterized by repetitive cycles of disease exacerbation (injury) and remission (healing). Complete epithelial wound healing predicts positive outcomes in IBD and is a major therapeutic target[17]. Despite the clinical relevance, the cellular origins of epithelial wound healing in acute colitis largely remain to be defined. Studies in biopsy injury models[18,19] have demonstrated the emergence of a wound associated epithelium of surface migratory cells overlaying the wound bed and which may derive from terminally differentiated colonocytes. However, it is not known whether the lineages of surface epithelial cells contribute to long-term repair of the epithelium. Moreover, although it is appreciated that the crypt architecture needs to be regenerated and duplicated through a fission process to restore proper colonic mucosal patterning, the intermediate mechanisms through which this complex sequence of architectural changes is executed, as well as the stem cells that power this process, remain to be defined in a setting of colitis. Multiple origins of injury-induced stem-cell activity corresponding to upregulation of specific molecular markers have been proposed – these include dedifferentiation (*Ascl2*)[20,21], reserve stem-cell activation (*Bmi1, Hopx*)[22-24], and reprogramming (*Clu, Ly6a*)[25-27]. Resolving these basic questions in the context of colitis and mucosal healing, and linking their answers to potential changes in clonality, could improve our fundamental understanding of IBD pathophysiology and reveal new therapeutic targets.

To help resolve these unknowns, we performed full-thickness imaging and three-dimensional reconstruction of murine fate-mapped colonic epithelium following acute injury and colitis. By varying the timing of induction of fate-mapping, lineage tracing provides quantitative access to both the architectural remodeling of whole crypts and the behaviors of single cells during colitis. By profiling the transcriptome of injured mucosa at single-cell resolution throughout repair, we could identify molecular signals associated with the evolution of progenitor cell function during regeneration. By testing the relative contributions of different crypt cells to the long-lived repaired epithelium, we could test whether regenerative potential was accessible to distinct populations of epithelial cells throughout the depth of the mucosa. Here we report that, during repair, there is a relaxation of the homeostatic crypt regenerative hierarchy. When coupled to unconstrained clonal proliferation of molecularly reprogrammed founder progenitor cells, this relaxation allows

rapid spread of epithelial cells throughout a labyrinthine network of transitional structures. This temporary period of wound-associated plasticity drives a pattern of field expansion governed by neutral cell dynamics.

Results

Sequential remodeling of the epithelium during acute colitis

Previous work[18] has demonstrated remodeling of colonic crypts at the edge of biopsy-induced focal ulcers; however, alterations to crypt morphology are less well understood in the context of more-diffuse injury and inflammation of IBD. To induce epithelial changes associated with mucosal healing in acute colitis, we administered dextran sulfate sodium (DSS) to mice over a period of 6 days (d), beginning on experimental day (exp d) 0. We then performed 3d imaging and *in toto* cellular reconstruction of distal colonic mucosa using a tissue clearing and imaging pipeline that we previously developed[28,29]. On the surface of the uninjured colon (Fig. 1A), we observed repetitive, orderly openings into crypt invaginations. After DSS treatment, we found that the distal epithelium underwent a stereotyped sequence of remodeling over a period of ~2 wks. At exp d 6, crypt openings were partially obscured by cellular migration on the luminal surface, and the crypts had either an atrophic or a split/furcated appearance (Fig. 1B). At exp d 9, there was extensive and diffuse ulceration, and surviving crypts exhibited a lateral (side-lying) appearance and were covered with a pseudostratified surface in some locations (Fig. 1C). At exp d 13, the mucosa resembled a labyrinth of shallow trenches (Fig. 1D). Proliferation mapping showed the presence of BrdU+ cells near the epithelial surface and deep within labyrinthine structures (Fig. S1A). By exp d 20, labyrinthine invaginations deepened and contained furrows suggestive of new crypt buds (Fig. 1E). By exp d 27, these crypt furrows/buds had deepened to give a split/furcated appearance reminiscent of widespread crypt fission (Fig. 1F). By exp d 84, the labyrinthine organization was generally no longer apparent (Fig. 1G). In proximal colon, the crypt structure was not visibly altered by DSS treatment at any of the measured timepoints. Together, these findings demonstrate dynamic DSS-induced changes in murine crypt morphology and branching that are common histological characteristics in human IBD[30].

Crypt lineages mix and re-compartmentalize during distinct stages of mucosal healing

We next questioned how the dynamic remodeling of the epithelium during colitis could be understood at the level of individual crypts. We tracked the lineages of clonally labeled crypts in high-resolution images of DSS-induced injury. We used a multicolored lineage tracing strategy formed by mating *Vil1*::CreERT2 mice with the *Rosa26*::Confetti reporter line to generate *Vil1*-Confetti mice; injection of mice with 1 mg tamoxifen resulted in a mosaic pattern of initial labeling in a minority of single epithelial cells on a background of widespread unlabeled tissue. Because of rapid crypt cell turnover, the initial labeling frequency is difficult to estimate[31]. However, based on the approximate frequency of recovery of labeled monoclonal crypts (described below), we estimate that ~8% of renewing crypt base epithelial cells were initially labeled. After a chase period of clonal proliferation and crypt cell turnover, the mosaic color pattern evolved into distinguishable color patches. To resolve crypt-level behaviors during healing, we made use of the property that, over a

period of around 8-12 wks, the natural turnover of cells within a colonic crypt leads to its monoclonal conversion[32,33]. Consistently, tamoxifen injection followed by a 12-wk chase in uninjured (homeostatic) conditions resulted in full labeling of ~8% of crypts with one of three equally random fluorophores (i.e., approximately 2.7% each cytosolic YFP, cytosolic RFP, or membrane CFP) (Fig. 2A, n=5 mice). In line with previous experience[33,34] with Confetti reporter mice in the alimentary tract, expression of the nuclear GFP fluorophore was seldom observed.

Following DSS-induced colitis, we found that sharp crypt clonal boundaries were temporarily lost and later re-established during repair. Multiply branched structures, observed early in repair, resulted from fusion of the upper thirds of labeled crypts with unlabeled neighbors (Fig. 2B). Likewise, the formation of labyrinthine trenches did not follow crypt clonal boundaries, as the trench-like structures were composed of the lineages of multiple crypts (Fig. 2C). The formation of new crypts in association with the labyrinth also occurred irrespective of clonal boundaries (Fig. 2D), but these crypts quickly became monoclonal and expanded to become clonal fields through sequential fission events (Fig. 2E). Consistent with this progressive process of crypt remodeling and reconstitution, the number of polyclonal crypt-like structures was transiently elevated during repair (Fig. 2F). The labeled clonal fraction within polyclonal structures was evenly distributed (Fig. 2G); thus, it is likely that new crypt buds are formed from the unbiased incorporation of cells from the trench. However, the overall fraction of polyclonal crypts was always <20% (Fig. 2F), consistent with rapid restoration of monoclonality through fission or clonal drift dynamics (Fig. 2H). Taken together, these data demonstrate that regeneration is neither instructed nor constrained by the crypt organization prior to injury. Instead, they implicate a mechanism involving the initial dissolution of crypts and lateral mixing and spreading of cells, followed by the rapid re-establishment of clonal fields likely through competition within the constrained spaces of the newly formed crypts.

To link these changes to temporal regulation of lateral migratory (elongation) and fission processes, we next quantified changes to the surface lateral extent (length), height, and fission index of labeled crypt lineages (Fig. 3A). The results demonstrated a multi-phasic pattern of crypt lineage remodeling after DSS treatment (Fig. 3B). In the "early" phase (exp d 6-8), crypt changes were dominated by lateral extension as part of their contribution to the polyclonal trench-like structures, with no evidence of crypt fission. In the "middle" phase (exp d 9-12), both lateral extension and crypt fission were detectable. In the "late" phase, (exp d 13+), the crypt changes were predominantly driven by fission as the lateral changes were minimal.

Notably, quantification of the statistical distribution of color patch lengths (Fig. 3C) and clone sizes by crypt number (Fig. S1B-E) suggested a unimodal (lognormal) size dependence, even after multiple rounds of injury (Fig. S1F-G). Such behavior stood in contrast to the bimodal size distributions that characterize the selective (non-neutral) expansion (Fig. S1H-J) and mutational profile (Fig. S1K-M) seen in a colitis-associated cancer model. These findings suggest that the size variability of individual clones seen in regeneration is not reflective of intrinsic heterogeneity in the fate potential of individual

crypts, but arises as the outcome of a stochastic regenerative process of an otherwise equipotent crypt population.

As the lateral elongation of crypts during early healing resembles a migratory process known as epithelial restitution, we tested the mediative roles of proliferative and migratory pathways. Treatment with DSS is associated with near-total loss of epithelial proliferation by exp d 3, which first resumes on DSS withdrawal at exp d 6[34]. We injected crypt-labeled mice at exp d 6 with pharmacological agents targeting topoisomerase (doxorubicin, inhibiting mitosis), Rho kinase (Y-27632, inhibiting collective sheet migration[35]), or TGFβ receptor signaling (GW788388), a key signal in restitution[36,37]. The nuclei-stained colons of all treatment groups showed evidence of merged crypt structures, demonstrating that local crypt fusion-like events remain a robust response at the pharmacological doses tested. However, the early lateral elongation of crypt color patches was severely impaired with doxorubicin (Fig. 3D-F). In contrast, the impairment by Y-27632 or GW788388 was weaker. Intriguingly, there was evidence that treatment with Y-27632 may have led to an increase in the survival of crypts, which could in turn reduce lateral crypt spread by limiting ulceration (Fig. 3G). We note that doxorubicin administered to uninjured mice reduced proliferative activity but conserved crypt structure in the distal colon while inducing severe degeneration of midcolon (Fig. S2). These results show that proliferative activity is required for significant lateral elongation of crypt lineages during early wound healing.

We next tested whether proliferative activity was required for the re-establishment of crypt organization in middle/late healing. We administered doxorubicin at exp d 11 and found significantly reduced crypt budding from color patches within the labyrinth structures (Fig. 3H-J). Taken together, these results support the conclusion that proliferative activity is the driver of clonal spread and morphogenesis during healing.

Statistical principles govern rapid establishment of clonal fields from founder progenitor cells

As cell proliferation appears to drive clonal evolution during repair, we interrogated the lineage relationships between proliferative epithelial cells during acute colitis and wound healing. We initiated lineage tracing at exp d 0, 6, 17, or 62 in *Vil1*-Confetti mice (Fig. S3) and followed the evolution of 40-60 color patches sampled from the injured area per animal over 3-4 weeks. Figure 4 demonstrates results from tracing initiated at exp d 6, the start of the proliferative response in repair. A comparison with other timepoints is shown in Fig. S3. Strikingly, we observed areas associated with profound clonal expansions, such that fields as large as 10-100 crypts were labeled by a single color (Fig. 4A). The mean clone perimeter (explained in Fig. S3B-C) indicated rapid growth in the short term (Fig. 4B). At all examined tracing timepoints during healing, the distribution of clone perimeters appeared approximately lognormal (Fig. 4C, S3D-F). Each clone was rapidly partitioned into multiple monoclonal crypts, which was evident in the early emergence of a "picket-fence" like distribution describing the convergence of the total number of crypts encompassed by each clone (crypt occupancy) onto integer numbers (Fig. S3D-F, S4A), and may be explained by the propensity of monoclonal conversion to occur in small crypt buds early in repair (Fig. S4B). These results demonstrate that repair lineages are underpinned by rapid clonogenic

expansion of a set of injury-associated progenitor cells, which we refer to as founder progenitor cells (FPCs), operating in tandem with morphogenesis.

We then questioned the origin of the lognormal-like clone size dependence and its implications on the spread of individual FPC lineages. Under normal homeostatic conditions, the intra-crypt dynamics of stem cell-derived clones is constrained locally, at the level of individual stem cells, and at the length scale of the crypt compartment. The neutral competition between neighboring stem cells leads to the local correlation in stochastic stem cell duplication and loss through differentiation which, at the clonal level, translates to a hallmark Gaussian-like dependence of the cumulative clone size distribution. This distribution persists until clones are altogether lost through differentiation, or crypts become monoclonally fixed. Then, at much longer timescales, the balance between crypt fission and fusion events is expected to lead to the neutral competition between neighboring clones resulting in an exponential-like distribution of clone sizes. By contrast, in the regenerative context, we find evidence of a much broader, lognormal-like, clone size dependence. Such behaviors occur not when there is local competition between stem cells or crypts, but when the dynamics become locally coordinated so that stem cells or crypts are more likely to duplicate if their neighbors duplicate, or become lost if their neighbors become lost (see STAR Methods). For example, these dynamics could arise if FPCs imprint proliferative behaviors onto their local daughter cells to enforce extensive lineage expansion.

To model this behavior, we made use of a minimal theoretical framework that could reproduce the lognormal distribution observed in Fig. 4C, indicating that the behavior of FPC lineages is locally coordinated (see STAR Methods). In stochastic simulations of locally constrained vs. coordinated modes of FPC expansion (Fig. 4D), we verified that the former predicts an exponential-like clone-size distribution (Fig. 4E-G), whereas the latter predicts lognormally distributed clone growth (Fig. 4H-J). Although there remain unknowns that preclude quantitative fits to clone-fate data, these simulations reinforce the basic phenomenon of locally coordinated expansion of FPC lineages and relaxation of the normal constraints of the homeostatic crypt organization to accommodate this expansion. Altogether, these findings are consistent with the emergence of an epithelial progenitor cell whose proliferative lineage can spread in a fluid-like manner to promote rapid wound re-epithelialization.

Progenitor cells exhibit an evolving transcriptional signature during mucosal healing

We next asked whether the FPCs exhibit distinct utilization of cell signaling pathways during repair. We therefore examined the transcriptomic diversity of epithelial cells in acute colitis using single-cell RNA-seq analysis of distal colonic mucosal cells before injury (exp d 0) and at early (exp d 6-8), middle (exp d 9-12), late (exp d 13-23), and very-late (exp d 42) stages of healing. This temporal partitioning roughly corresponds to periods of change in epithelial morphology. We also examined pooled single-cell suspensions from inflamed colonic mucosa of $Il10^{-/-}$ mice. To boost statistical power, we merged profiling performed in 2 batches here with our previously published dataset[34] of distal colonic mucosal cells near the anorectal junction, redacting cells of the keratinocyte lineage. After merging all samples, normalization, batch correction, filtering, and clustering (Fig. 5A, Fig. S5A), we

obtained 68,224 single-cell transcriptomes comprising defined populations of epithelial, mesenchymal, and immune cells (Table S1). Both DSS-treated and $Il10^{-/-}$ samples were associated with increased recovery of immune cells; however, innate immune cells were primarily recovered from DSS-induced colitis and lymphocytes from $Il10^{-/-}$ colitis (Fig. 5B).

We performed time-series analysis on epithelial cells during DSS-induced colitis and healing. After temporarily redacting the $Il10^{-/-}$ cohort, the 15,525 remaining epithelial cells comprised 7 clusters that recapitulated key absorptive, secretory, and progenitor cell populations (Fig. 5C, S5B and Table S2) that we validated with histological stains (Fig. S5C-E). During homeostasis, the stem cell population at the crypt base was marked by expression of *Gpx2*, and a second population of progenitors extending higher up the crypt demonstrated enriched expression of *Gsdmc4*. A reversible change in the global transcriptomic profile of cells during healing could be detected upon dimensional reduction (Fig. 5D). During early healing, epithelial cell composition was relatively enriched for non-secretory differentiated cells (Fig. 5E). Furthermore, consistent with previous reports[26,27,38], high expression of the *Ly6a* (*Sca1*) interferon-inducible marker of injury-associated epithelium was found in the early and middle stages of healing (Fig. 5F) and was localized to crypts and surface cells in proximity to ulcerations (Fig. 5G). Using the levels of *Ly6a* as a gate, we could therefore focus our analyses on the cells closest to the injury. The expression profile of *Ly6a*^{hi} cells correlated with enrichment of interferon-γ (*Ifng*) signaling (Fig. S5F-G) and overlapped with fetal intestinal signals[39] (Fig. S5H). Epithelial cells expressed high levels of the *Ifng* receptors in conjunction with lymphocytes expressing the *Ifng* ligand (Fig. S5I). During early healing, >60% of cells were *Ly6a*^{hi}, a proportion that gradually fell as healing progressed (Fig. 5H). The *Ly6a*^{hi} epithelial cells were not a simulacrum of the cell diversity of normal epithelium. Instead, they were relatively depleted of secretory cell lineages (Fig. 5I). The high prevalence of differentiated *Ly6a*^{hi} cells during early healing was reflected by a reduced Simpson diversity index at this stage (Fig. 5J). Critically, proliferative cells marked by high expression of survivin (*Birc5*) were exclusively *Ly6a*^{hi} during early healing (Fig. 5K). Taken into consideration with our fate-mapping studies (Fig. 4), these results are consistent with the emergence of proliferative progenitor cells (i.e., FPCs) within a relatively unform *Ly6a*^{hi} regenerative epithelium during early healing.

To identify putative FPC-specific genes, we divided each epithelial cluster by *Ly6a* expression level and computed specificity scores for genes marking the *Ly6a*^{hi} subset of the *Gpx2*-enriched stem cell population (Fig. 6A, Table S3). These genes represented significant enrichment of mitotic pathways (Fig. 6B), consistent with the relatively unconstrained proliferative phenotype of FPCs identified by modeling studies (Fig. 4). FPCs were marked by transcripts such as *Ass1*, a member of the arginine biosynthetic pathway, and *Sulf2*, a sulfatase that modulates heparan sulfate signaling (Fig. 6C-D, S5J), which were expressed only at low levels in *Ly6a*^{lo} stem cells. Although *Clu*, a "revival" stem cell marker[25], was also highly enriched in *Ly6a*^{hi} stem cells, its expression was also found in non-stem cells, and its upregulation was only detected in late healing and after; thus, it did not form part of the FPC signature (Fig. 6C, S5K-L). Stem cell markers *Lgr5* and *Hopx* were not specific for *Ly6a*^{hi} vs. *Ly6a*^{lo} stem cells (Fig. 6C). Thus, FPCs do not neatly correlate to

some reported populations[24,40] of injury-induced progenitor cells and instead generically upregulate aspects of proliferation and metabolic remodeling.

We next tested whether the emergence of the FPC signature could be detected over time in the epithelium as a whole. We identified genes whose expression evolved with time (Table S4) and performed unsupervised clustering to discern 6 groups based on their temporal pattern (Fig. 6E). FPC genes were represented in 2 groups (Table S5): one ("rebound-middle") which consisted of genes that had appreciable expression before injury and demonstrated re-expression in middle healing, and another ("rise-middle") that had injury-specific expression beginning in early healing and peaking during middle healing. Pathway mapping (Fig. 6F) showed that rebound-middle genes consisted of proliferative pathways, but that rise-middle genes consisted of pathways of metabolic upregulation including mTOR activation, glycolysis, oxidative phosphorylation, and cholesterol homeostasis. The pathway mapping also supported the multiphasic nature of healing elucidated in imaging studies (Figs. 1-3). The early lateral elongation phase was characterized by epithelial-mesenchymal transition-like changes, *K-Ras* signaling, and apoptosis, whereas the middle phase showed proliferative and metabolic changes (Fig. 6F). Although 9 genes including *Clu* exhibited peak expression during late healing, these were not sufficient to run pathway analysis. All healing phases demonstrated upregulation of an epithelial immune response, in contrast to epithelial homeostasis which exhibited enriched Hedgehog and endocrine signaling. Thus, within a background of immune-induced signaling, the proliferative and metabolic FPC signature first emerges in early healing and grows to predominate the epithelial transcriptome by middle healing.

To facilitate the derivation of a small FPC gene signature to evaluate its presence in other contexts, we leveraged the time-resolved analysis to select *Ly6a^{hi}* stem cell markers that overlapped with the rise-middle temporal pattern. This resulted in 20 genes (Table S6) that demonstrated enrichment for splicing pathways, serine metabolism, and mTOR signaling (Fig. 6G). We next tested whether standard distal colonic epithelial organoid culture might recapitulate some aspects of FPCs, because early stages of intestinal organoid culture, regardless of their cell of origin, are characterized by the similar presence of *Ly6a^{hi}* cells within growing spheroids[41]. Treatment of colonic organoids with inhibitors against some signals upregulated in FPCs, such as FOXM1-mediated transcription (Fig. 6B), reduced spheroid size; however, pharmacological modulation of mTOR, part of the FPC conservative signature (Fig. 6G), had no effect (Fig. S5M-N). Administration of doxorubicin and the TGFβ receptor I inhibitor SB525334, which impaired lateral extension in vivo (Fig. 3F), potently suppressed growth in vitro (Fig. S5M-N). Thus, only some aspects of FPCs are modeled in standard organoid conditions. In contrast, stem cells in *Il10^{−/−}* epithelium showed significant upregulation of the FPC conservative gene signature (Fig. 6H). Furthermore, retrospective analyses of a published human IBD dataset[42] revealed enrichment of the FPC signature in progenitor epithelial cells and marked upregulation in inflamed biopsies in some patients (Fig. S6). Thus, the FPC expression profile may represent a conserved progenitor cell response in colitis.

Long-term contribution of surface-cell lineages to repair

Our clonal fate-mapping and single-cell transcriptomic experiments support conversion of the epithelial cell population to a more-homogeneous regenerative state in early repair, followed by the emergence of a highly proliferative cell population that then drives epithelial expansion. We next investigated the extent to which the imprint of the homeostatic crypt hierarchy affected which cells could become FPCs. We validated[43] loss of the *Lgr5+* stem cell population in DSS colitis. However, like findings in irradiated small-intestinal epithelium[20], the short-term progeny of *Lgr5+* cells traced into regenerative crypt fields (Fig. S7A-G). These experiments support that regenerative epithelium is derived from lineage descendants of homeostatic epithelium.

To determine whether epithelial cells throughout the depth of the injured mucosa could contribute to the FPC population, we performed lineage tracing from targeted cell populations. *Lrig1* has been shown to mark epithelial cells in the lower half of the colonic crypt[44], and tracing from *Lrig1+* cells in homeostasis resulted in full crypt labeling of the distal colonic epithelium (Fig. S7H). Moreover, tracing from the *Lrig1+* population from exp d 6 of DSS-induced injury acutely labeled cells in the lower half of the mucosa and, after 4 wks, labeled full crypts in a patchwork pattern across the mucosal surface (Fig. S7I-K). Thus, basal epithelial cells represent one potential origin of repair-associated fields.

To test whether surface epithelial cells also contribute to long-term labeling of repair epithelium, we initiated tracing in *Krt7*::CreER;*Rosa26*::mTmG mice[45]. Although squamous cells at the anorectal junction are strongly labeled in these mice[34], we serendipitously observed sporadic and spatially distinct labeling restricted to upper crypt cells in the colon in homeostasis (Fig. 7A). The label was not found except in anal squamous cells after a 1-wk or 4-wk chase (Fig. 7B-C), consistent with shedding of upper crypt cells due to normal epithelial cell turnover. However, following DSS treatment, the *Krt7+* lineage expanded near the luminal surface (Fig. 7D) and later represented full crypts in repair-associated fields after 4 wks (Fig. 7E). Similar results were obtained with tracing initiated using the *Krt20* upper-crypt cell marker (Fig. S7L-R). Quantitative comparison of these lineage tracing results (Fig. 7F) supports that reprogrammed epithelial cells throughout the depth of the colonic mucosa can serve as cells-of-origin for FPCs and long-term repair. Analysis of single-cell transcriptomic data (Fig. 5,6) demonstrated upregulation of the FPC proliferative gene signature within *Ly6a^hi* subsets of differentiated colonocytes (Fig. 7G), consistent with overall plasticity and access to proliferative fates in differentiated cells through reprogramming.

Discussion

Using a combination of 3d imaging, quantitative lineage tracing, and single-cell transcriptomics, we demonstrate that acute colitis induces epithelial regeneration that is characterized by massive clonal field expansion. These field effects are driven by the specialized dynamics of normal wound healing occurring through multiple stages (Fig. 7H). DSS-induced injury temporarily freezes epithelial proliferative activity. The regenerative process reprograms the epithelium into an injury-adapted state in which crypts first lose their structural integrity, becoming fused into labyrinth-like structures with channels that extend

into the injured region. Repair is then powered by the emergence of founder progenitor cells committed to a proliferative state enabling rapid spread of lineages. Finally, crypts then re-initiate and fission within the channels to re-establish the characteristic glandular organization of the colon. The dynamic changes in crypt morphology are similar to the architectural distortions observed in human IBD.

Field expansion is a hallmark pre-oncogenic change. The traditional model for field cancerization involves the gradual but continuous lateral spread of mutant epithelial stem cells that harbor a fitness advantage. In this study, the elucidated repair-related mechanism does not require that cells have a genetically acquired fitness advantage. Moreover, it describes field formation linked to flares of acute injury and colitis and argues for a punctuated temporal model of field expansion, in which long periods of overall clonal stability (e.g., remission) could be perturbed by sudden clonogenic events associated with wound healing (e.g., flares) where the compartmentalization afforded by the crypt organization is temporarily disassembled. We note that FPCs could contain passenger mutations that could accumulate over multiple flares of injury and healing, which could ultimately drive tumorigenesis, and that certain mutations could promote FPC specification or activity. Thus, although specific mutations are not required or linked to FPCs, mutations can still play important roles in the overall parameters of field formation.

Molecular profiling of colonic epithelium demonstrates injury-induced reprogramming of epithelial cells. The inflammatory microenvironment likely plays a major role in this process. Reprogrammed epithelium expressed high levels of interferon targets, consistent with the overall importance of global interferon signaling for repair[46]. Cellular phenotypes resembling differentiated non-secretory cells were predominant during the early healing stage and may resemble the "adaptive cellular differentiation" identified in villus regeneration[47]. These cells may be undertaking restitution, classically defined by the rearrangement of F-actin filaments to generate protrusions facilitating cell migration[48], and as such may upregulate signals common to epithelial-mesenchymal transition. However, at the wider length-scale characterizing crypt elongation, proliferative signals were required for appreciable lateral movements of clonal lineages. Moreover, although we noted reduction in secretory cell lineages in early healing, secretory cells from neighboring normal epithelium could still contribute in principle to repair through luminal or systemic secretion of regulatory signals.

The multistage progression of healing within the reprogrammed state is reflected by both our imaging and our transcriptomics studies. A critical question remains as to what drives the "switch" between the early, less-proliferative stage and the later dominance of FPCs. Within the transcriptomes of the FPCs themselves, there are clues that suggest metabolic remodeling and signals related to the regulation of splicing – however, the specific triggers for these changes remain to be elucidated. Given a multitude of studies identifying roles of microbes and host stromal cells in epithelial repair (summarized here[17]), it is likely that some of these signals are governed by non-cell-autonomous cues. However, a possible explanation given that FPCs can originate from throughout the wound epithelium is that initial FPC emergence is functionally random.

We find that plasticity is a primary feature of mucosal healing in acute colitis. The plasticity is evident in two major ways. First, the normal crypt structure is eroded, allowing distinct units of regeneration that are normally separated to merge. Second, FPCs can be specified from surface epithelial cells that would normally be terminally differentiated, although it is possible that different celltypes may revert to FPCs with distinct probabilities. We believe that one potential evolutionary advantage to the loss of crypt boundaries is to accommodate the fluid-like spread of FPC lineages. If the spread of FPCs were constrained by structural elements, we would not have expected to observe a lognormal distribution of clone sizes. By temporarily relaxing the strict boundaries of crypts, FPCs can expand in a multiplicative manner to facilitate rapid re-epithelialization across the extent of the colonic surface. However, once sufficient re-epithelialization is achieved, it is important to restrict this plasticity. The re-establishment of crypt structure and hierarchy in late healing represents an important step in this process. Intriguingly, we found that the revival stem cell marker *Clu* is upregulated in this late phase, which could implicate it in mediating the specific events needed to return the epithelium to homeostatic signaling.

Multiple models, including the activation of reserve stem cells, reverse differentiation, and reprogramming, have been proposed to underpin the formation of injury-adapted progenitor cell populations[49]. Some of these findings may depend on the injury model used[23,38,40]. Here we find elements of each mechanism that could enable their partial reconciliation. In DSS-induced colitis, the adoption of a distinct transcriptional state with altered cellular diversity supports reprogramming. The ability of cells throughout the depth of the mucosa to become FPCs supports dedifferentiation. The dynamics of repair result in profound amplification and clonal fixation of single-cell lineages. Through integrated analysis of epithelial cell clonality, lineage ontogeny, and spatial remodeling, we find that the challenge of acute colitis activates broad plasticity mechanisms and a key clonogenic progenitor cell population to promote rapid healing. These FPCs could represent an unrealized therapeutic target to support mucosal healing in colitis.

Limitations of the study

Although FPCs were functionally prominent in healing from DSS-induced colitis, and key aspects of their molecular signature were also found in *Il10*$^{-/-}$ colitis and in some IBD patients, it remains to be determined whether these injury-induced stem cells expand with similar unconstrained dynamics in human IBD or in other preclinical IBD models. In the setting of chronic inflammation, it will be important to resolve whether FPCs persist or whether their activity fades after the initial onset of disease. Furthermore, it remains a key goal to determine which aspects of FPC activity are driven by specific signals in the inflammatory milieu. We also have not detailed the temporal changes in mesenchymal cell populations, which may be driving some of the morphological changes in the mucosa. Live imaging will help to resolve how spatially dynamic parameters such as an individual crypt's distance to the wound bed might affect its regenerative program; at present this cannot be ascertained from static images because the exact prior location of the wound bed cannot be defined. Although we profiled >15,000 epithelial cell transcriptomes during mucosal healing in the DSS colitis model, the relatively rarity of the early FPC population limits the sensitivity in detecting potential driving pathways of progenitor cell specification.

STAR Methods

RESOURCE AVAILABILITY

Lead Contact—Further information and requests for resources and reagents should be directed to and will be fulfilled by the lead contact, D. Brent Polk (dpolk@ucsd.edu).

Materials Availability—This study did not generate new unique reagents.

Data and Code Availability

- Single-cell RNA-Seq data have been deposited in NCBI GEO and are publicly available under the accession number GSE193342. Microscopy data reported in this paper will be shared by the lead contact upon request.

- All original code has been deposited on Github (https://github.com/stalepig/2021-stem-cell-clonality) and is publicly available (DOI: 10.5281/zenodo.8201653).

- Any additional information required to reanalyze the data reported in this paper is available from the lead contact upon request.

EXPERIMENTAL MODEL AND STUDY PARTICIPANT DETAILS

Mice—Mice were maintained humanely in accordance with the rules and regulations of the Institutional Animal Care and Use Committee at Children's Hospital Los Angeles (protocol #288) and at the University of Chicago (protocol #72668). Adult mice were divided by sex and co-housed in groups of up to 5 animals per cage. Mice of both sexes were used for experimentation. For general husbandry, mice were fed an irradiated diet and offered water through a drinking valve *ad libitum*, and maintained on a 12 h light-dark cycle. Mice were co-housed after weaning at 3 wks-old, and experiments were begun at 8 wks-old. To account for cage-specific variability, mice involved in a timeseries experiment were dissected such that each timepoint contained mice from different cages. Mice were euthanized by exposure to isoflurane anesthesia, followed by cervical dislocation.

Transgenic mice were obtained from Jackson Laboratory: *Lgr5*::EGFP-IRES-CreERT2 (stock #008875), *Lrig1*::CreERT2 (stock #018418), *Rosa26*::Confetti (stock #017492), *Rosa26*::LSL-tdTomato ("Ai14" – stock #007914), *Il10*$^{-/-}$ (stock #002251), and *Rosa26*::mTmG (stock #007676). *Krt7*::CreERT2 mice were a kind gift from Jianwen Que (Columbia University, USA). *Krt20*::CreERT2 mice were generously provided by Andrew McMahon (University of Southern California, USA). *Vil1*::CreERT2 mice were donated by Sylvie Robine (Institut Curie, France).

Retrospective analyses of human IBD patients—Transcriptomic analyses of single-cell RNA-Seq data from IBD patients was performed with a previously published dataset[42].

Colonic epithelial organoids—Organoids were isolated from the distal colons of 8-wk-old C57Bl6/J wildtype mice using a previously described mucosal isolation procedure[50]. Organoids were grown from both male and female mice. Briefly, colons were isolated

and the distal 3-cm opened, cleaned of fecal matter, and washed with HEPES-buffered saline. The mucosa was freed from the underlying muscle layer by fine dissection under a stereomicroscope. Mucosal tissue was minced and dissociated by shaking at 175 rpm for 30 minutes at 37°C in a pre-warmed solution containing 0.2 Wunsch units/ml Liberase TM and 200 Kuntz units/ml DNase I in HEPES-buffered DMEM/F12. Tissue fragments were triturated, passed through a 100 μm nylon filter, and washed twice with 10% fetal bovine serum in HEPES-buffered DMEM/F12. The cell suspension was additionally passed through a 30-μm filter to achieve uniform plating size. The cell pellet was resuspended in 50 μl DMEM/F12 per donor mouse and mixed with 200 μl of cold Matrigel. The Matrigel:cell solution was aliquoted throughout a 24-well plate in 20 μl gel/well domes. After 10 min of gel solidification at 37°C, each well was overlaid with 0.5 ml Mouse Intesticult media (STEMCELL Technologies) supplemented with 50 μg/ml Primocin (Invivogen). Cultures were maintained at 37°C. Media was refreshed every 3 days.

METHOD DETAILS

Colitis and colitis-associated cancer—Dextran sulfate sodium (DSS)-induced colitis was administered as described previously[29,51]. DSS (36-50 kDa) was purchased from MP Bio (0216011091). DSS was added to the drinking water to 3% w/v concentration for 6 d (from exp d 0 to exp d 6). During this period, DSS-supplemented water served as the only source of water for the mice.

To apply multiple rounds of DSS, each round consisted of a 6 d treatment with 3% DSS followed by 15 d of regular water. To induce tumorigenesis in the azoxymethane (AOM)-DSS model, mice were first injected intraperitoneally with 0.375 mg AOM (Sigma, A5486), and 1 wk later the mice began treatment with 3 rounds of DSS.

Pharmacological treatments of mice—Stock solutions of 20 mg/ml tamoxifen were prepared by dissolving tamoxifen in corn oil at 60°C. Stock solutions of doxorubicin, SB525334, and Y-27632 were prepared by creating a 50 mg/ml solution of each drug in DMSO. On the day of administration, for each mouse, 10 μl of this stock solution was added to 30 μl of PEG300, which was in turn added to 5 μl of Tween-80, and finally topped to the target 100 μl injection volume with water. Agents were administered via intraperitoneal injection.

Organoid treatments—Stock solutions at a concentration of 10-50 mg/ml in DMSO were prepared for MHY1485, nifuroxazide, rapamycin, Y-27632, SB525334, FDI-6, and doxorubicin. A second stock solution was generated at 100x concentration in DMEM/F12. Treatments were applied by adding 5 μl of the second stock to the 0.5 ml of the Intesticult media already in the well. Organoids were imaged on an Olympus stereomicroscope with a mounted camera.

Lineage tracing experiments—Lineage tracing was induced by a single intraperitoneal injection of 0.1-1 mg tamoxifen per mouse. Animals were euthanized and colons dissected at >2 d after induction. Colons were processed as previously described[29]. Briefly, colons

were fixed in 4% paraformaldehyde and freed of the muscle layer. The mucosal layer was stored at −20°C in 20% sucrose/PBS until staining, clearing, and imaging.

Immunohistochemistry—Immunohistochemistry was performed according to standard procedures on paraffin-embedded sections of the mouse colon. Antigen retrieval was performed for 20 min in a pressure cooker using a buffer containing 10 mM sodium citrate and 0.05% Tween-20, titrated to pH 6.0. Primary antibodies used were mouse anti-GSDMC4 (Aviva Systems Biology, ARP96264_P050), rabbit anti-MGAT4C (Proteintech, 17841-1-AP), rat anti-BrdU clone BU1/75 (Abcam, ab6326), and rabbit anti-KRT7 clone EPR17078 (Abcam, ab181598). Revelation of staining was performed using ImmPRESS Polymer Reagents (Vector Laboratories, MP-7452, MP-7402) and the VIP substrate kit (Vector Laboratories, SK-4605). Sections were counterstained with methyl green.

In situ hybridization—Tissue hybridization studies on paraffin-embedded mouse colon sections were performed using RNAScope HD 2.5 – Brown kits (Advanced Cell Diagnostics / Biotechne, 322310) according to the manufacturer's instructions. The following probes were purchased from Advanced Cell Diagnostics: Mm-*Ly6a*-C1, Mm-*Sulf2*-C1, Mm-*Ass1*-C1, Mm-*Gpx2*-C1, and Mm-*Clu*-C1. Staining was revealed using the DAB substrate kit (Vector Laboratories, SK-4103). Sections were counterstained with hematoxylin and blued with 0.2% ammonium hydroxide (pH 10).

EdU/BrdU double staining—Double labeling and staining were performed as previously described[34]. In brief, we performed intraperitoneal injections with 2.5 mg EdU (Cayman, 20518) 24 h prior to dissection and 2.5 mg BrdU (Abcam, ab142567) 2 h prior to dissection. EdU was revealed in thin sections after heated acidic antigen retrieval using the following reaction cocktail applied for 30 min at room temperature: 2 mM $CuSO_4$, 10 mM THPTA, 2 μM Cy3 azide (Click Chemistry Tools, AZ119-1), and 100 mM ascorbic acid in Gomori buffer (pH 7.4). Immunostaining for BrdU was performed after EdU revelation. In whole-mount specimens, the iDISCO[52] procedure (methanol) was performed to permeabilize the specimen, and the EdU revelation was performed overnight at room temperature. Acid-nicking was performed with 2N HCl at room temperature for 90 min, and antibodies against BrdU were subsequently applied.

Deep Mucosal Imaging (DMI)—Samples were cleared and imaged according to the previously developed DMI pipeline[28,29]. In summary, a stored 3-cm-long piece of colonic mucosa was defrosted and placed in 2 ml CUBIC-1 solution supplemented with 1:1,000 dilution of 2% methyl green. The methyl green stock solution was purified of contaminating crystal violet dye by 6 repeated phase separations with chloroform. The samples were incubated at room temperature with gentle rocking in this clearing and staining solution for 1-7 d. Samples were directly moved with 150 μl of the clearing/staining solution and wedged between two #1 coverslips for imaging on an LSM700 confocal microscope (Zeiss), an SP8 confocal microscope (Leica), or an RS-G4 upright slide-scanning confocal microscope (Caliber I.D.). Images were acquired overnight by tiling of z-stacks through the whole tissue. The z-plane resolution was determined automatically (between 2-7 μm

thickness). We used both 10X/0.45NA and 20X/0.8NA air objectives. After imaging, the sample was returned to storage at −20°C in 20% sucrose/PBS.

To perform co-staining for KI-67 expression within fluorescent protein-labeled lineages, we incubated the tissue at room temperature for 3 d in CUBIC-1 without methyl green. Background signals were blocked with a solution of 5% normal goat serum and 0.3% Triton X-100 in PBS overnight. The tissue was incubated with the primary antibody solution containing eFluor 570-conjugated rat anti-KI-67 (eBioscience, 41-5698), normal goat serum, and Triton X-100 in PBS for 4 d. After successive washes, the tissue was cleared in CUBIC-2 supplemented with 1:5,000 dilution of 2% methyl green for 2 d, and subsequently mounted and imaged within this clearing solution.

Single-cell RNA sequencing—Distal colonic mucosal cells were isolated and sequenced in 2 batches that were later combined for analysis. In batch 1, 56 C57Bl/6J mice of 6 wks-old were purchased from Jackson Laboratory. Mice were acclimated to the animal care facility at CHLA until 12 wks-old. Eight mice were dissected, and their colons isolated and pooled, to represent the uninjured ("exp d 0") library sample. The remaining mice were treated with 3% DSS for 6 d. Groups of 8 mice were serially dissected and their colons pooled per library, for a total of 6 libraries at exp d 6, 9, 12, 16, 19, and 23. A separate cohort of 8 *Il10*$^{-/-}$-mice was purchased from Jackson Laboratory and dissected at ~1 year of age. These mice had severe colitis at the time of dissection. These pooled mice represented the "IL10" sample library. In batch 2, 9 C57Bl/6J mice of 6 wks-old were purchased from the Jackson Laboratory and acclimated to the animal care facility at the University of Chicago until 12 wks-old. Mice were treated with DSS and cells isolated at exp d 7, 11, and 18, with 3 mice pooled for each timepoint library.

In each animal, the distal 3-cm of the colon was isolated. The anal junction and squamous neo-epithelium of the colon were removed. The mucosal layer was manually freed from the muscle layer with fine dissection scissors. The intact mucosal layers were minced and digested as previously described [50]. Briefly, tissue was incubated in a pre-warmed DMEM/F12 solution containing 0.2 Wunsch units/ml Liberase TM, 200 Kuntz units/ml DNase I, and 15 mM HEPES for 30 min at 37°C with agitation at 175 rpm. The digestion reaction was neutralized with 2 washes with a DMEM/F12 solution containing 10% v/v heat-inactivated fetal bovine serum (HI-FBS) and 15 mM HEPES. The tissue was triturated and filtered through a 70-μm nylon mesh filter, then treated for 5 min with 10 ml chilled red blood cell (RBC) lysis solution. Tissue was washed with HEPES-buffered saline (HBS)[53] supplemented with 1% w/v bovine serum albumin (BSA), spun at 300 rcf for 5 min to collect cells, and filtered to a single-cell suspension through a 40-μm nylon mesh filter. The EasySep Dead Cell Removal Kit (STEMCELL Technologies, 17899) was used according to the manufacturer's instructions, with a 5 μl antibody cocktail volume, followed by bead conjugation and magnetic separation for 10 min at room temperature. Live cells were washed with HBS+1% BSA. Viability was confirmed to exceed 90% with trypan blue staining and counting on a hemocytometer.

In batch 1, cells were resuspended to 0.5 ml in a solution containing 90% HI-FBS and 10% DMSO. Cells were frozen to −80°C at an approximate rate of −1°C/min. All samples were

collected and frozen for further simultaneous processing. Frozen samples were shipped to the DNA Technologies Core at UC Davis (California). Samples were washed with phosphate buffered saline prior to loading. Viability was confirmed to exceed 75% for all 8 samples. In batch 2, samples were freshly loaded on the day of dissection. All samples were profiled on the Chromium system of 10X Genomics with a targeted recovery of 10,000 cells/sample. Libraries were sequenced on the novaSeq platform. Transcript abundances were quantified using the default options of cellranger 3.0.0 (https://support.10xgenomics.com/single-cell-gene-expression/software/pipelines/latest/what-is-cell-ranger). The recovery of cells, prior to filtering of doublets and squamous cells, from batch 1 ranged from ~2,900 to 7,000 cells per library; from batch 2 the recovery was from ~8,600 to 12,100 cells per library.

gDNA isolation for exome sequencing—Male C57Bl/6J mice of 8 wks of age were treated with water (n=5 mice), DSS (n=5 mice), or AOM/DSS (n=10 mice). Mice were dissected 4 wks after the end of the final DSS treatment. The distal colonic mucosa was freed from the muscular layer and lesions (colitis and/or tumors) isolated under a stereomicroscope. Genomic DNA was purified from the lesioned tissue using the PureLink Genomic DNA Mini Kit (ThermoFisher Scientific, K182001). Samples were sequenced by MedGenome, Inc (California) using a mouse exon enrichment kit to a targeted coverage of 50X. Sequences were delivered as FASTQ files.

QUANTIFICATION AND STATISTICAL ANALYSIS

Whole-mount imaging files—Images were typically >15 GB and were analyzed using DMI routines available at https://github.com/stalepig/deep-mucosal-imaging. For images acquired on the Zeiss confocal microscope, the "Walk_faster" routine was used to assemble slices into 3d stacks. Full resolution browsing was enabled through the "Import_image" routine. Estimates of surface area involvement of lineage tracing were obtained using the "Count_bright_pixels_in_ROI" routine. The standard ROI tools in ImageJ 2.0.0-rc-59/1.51j were used to measure distances and clone sizes. For images acquired on the Caliber confocal microscope, the pixel data were downsampled to 8 bits and the scaled images reconstructed using the "Batch_walk_faster_Caliber" routine. For images acquired on the Leica confocal microscope, 3d stacks were assembled and stitched using the "Explode_LIF_into_tiles" routine.

Clonal analysis—Images were reconstructed as 3d stacks using the DMI software pipeline. A color patch was defined as a contiguous region of fluorescent cells of a single color within 3d space. Within images, we defined the affected area as an area in which crypts either show evidence of atrophy (i.e., expanded and circularized lumen), are overlaid by or embedded within wound channels of the labyrinthine network, or are part of a regenerative cluster (focus) of crypts. An unaffected region was defined as an area of at least 15 x 15 crypts of grossly normal morphology. These areas were visualized by imaging the tissue labeled with a nuclear dye (methyl green).

As shown in Fig. 3A, to calculate the lateral extent of the color patch, a maximum intensity projection was calculated, and a line was drawn that measured the maximal end-to-end distance of the patch surface. To calculate the depth of the patch, the z-position of the

deepest crypt base was subtracted from the z-position of the highest surface slice. The number of crypts per color patch was counted as the number of circular invaginations into the basal lamina propria. We measured the 10 longest/deepest/most fissioned color patches per animal. Data points shown in Fig. 3B represent the median of these "leading" crypts per animal. The clonality of crypts (in Fig. 2F,G) was assessed by visualizing the full crypt, from its base to its luminal opening onto the mucosal surface or into a wider wound channel. If the crypt was fully labeled by a single color, then the crypt was scored as monoclonal. However, if the crypt exhibited >1 color or was only partially labeled by a single color, then it was scored as polyclonal. We note that this method of quantification will underestimate the frequency of crypts of polyclonal origin due to their fusion near the lumen. For Figs. 3C, S1E, and S1G, all color patches were counted in the affected region. In Fig. S1I-J, the sizes of tumor clones were measured in 2d at the z-depth yielding the largest surface area for each clone.

In Figs. 4C and S3, we calculated the sum of the basal circumferences of each of the crypts within a color patch. The crypt base was located from 3d images. The perimeter was measured at the z-depth representing the maximum circumference of the crypt. The clonal occupancy was defined as the fraction of the crypt circumference that is labeled. When a color patch contains multiple crypts, the total occupancy is the sum of the individual occupancy values of the constituent crypts. In each mouse, we counted 40-60 color patches that were located within the injured region. The density distributions of each mouse were computed separately and then averaged together to obtain the representative distribution of the population.

Mouse single-cell transcriptomic data—Downstream analyses were primarily performed using monocle3[54] (https://cole-trapnell-lab.github.io/monocle3/). For analysis of mucosal cellular composition, count matrices were combined from the experimental batches 1 and 2. This was supplemented with count matrices from our previous analysis (exp d 0, 7, and 42) of the anorectal junction and distal colon[34]. Cells of the keratinocyte lineage (*Krt14+* and *Col17a1+*) were filtered out. Cells with fewer than 100 UMI counts were filtered out. All samples were merged into a CellDataSet object, and batch correction[55] was performed using a mutual nearest neighbor alignment technique[55] circumscribed in the align_cds() function. The count matrix was normalized by the per-cell count total and subsequently log-transformed (preprocess_cds() and reduce_dimension() function defaults). The top 100 principal components were used for dimensional reduction and uniform manifold approximation and projection (UMAP). Clustering of cells was performed using the leiden algorithm with automatic detection of the resolution (cluster_cells() function defaults).

The top_markers() function of monocle3 was used to identify markers of each cell cluster. This function computes a Jensen-Shannon specificity for each gene in each cluster (Table S1). The top 5 markers, as measured by their specificity, r^2 value (in a linear regressor used to determine statistical significance of the marker), and marker score (a combination of specificity with overall expression level in the cluster), were used to manually annotate the cluster with a known cellular identity. For hematopoietic cells (*Ptprc+*), the top markers were compared to signatures available at the "My Dataset" portion of the Immunological

Genome Project[56] (http://immgen.org) to identify subclasses of lymphoid and myeloid cells. Epithelial cells were *Krt8+*. Distinct but small clusters with simultaneous, moderate expression of epithelial and either immune or mesenchymal (e.g., *Fn1*) markers were considered heterotypic cell-cell fusions; these cells were removed from the analysis.

Epithelial cells were subsetted for additional analysis. The count matrices were then re-normalized, and batch correction and dimensional reduction repeated, prior to clustering and cell-type assignment (Table S2). DSS-treated samples were separated from *Il10*^{−/−} samples for timeseries analysis. Timepoints were binned into groups that represented the before-injury (exp d 0) and early (exp d 6-8), middle (exp d 9-12), late (exp d 13-23), and very-late (exp d 42) stages of healing. These timepoints approximate the stages observed in imaging studies of healing (Figs. 1-3).

To identify *Ly6a*^{hi} cells, we examined the histogram of *Ly6a* raw expression and gated the epithelial cells such that 25% of the cells were considered *Ly6a*^{hi}. To identify genes whose abundance changes were correlated with *Ly6a* expression, we computed the mean normalized abundance value for each gene among the epithelial cells that were classified as *Ly6a*^{hi} or *Ly6a*^{lo}. This was performed for the epithelial cells as a whole (Fig. S5F-H) or cluster-by-cluster (Fig. 6A). The specificity score (*Spec*) of each gene g is calculated over its expression in individual clusters c_i as:

$$Spec_g = \frac{Expr_g(c_1) - Expr_g(c_2)}{\overline{Expr_g} + 0.001}$$

Where $Expr_g(c_1)$ is the expression level of gene g in cluster c_1, the cluster in which it exhibits highest expression, and $Expr_g(c_2)$ is the expression in the cluster for which gene g exhibits the second-highest expression, and $\overline{Expr_g}$ represents the median expression of gene g over all clusters. Genes with specificity score >1.5 were retained for further analysis and integration with time-resolved data.

To analyze changes in gene expression over time (Fig. 6E), the mean value of each gene's raw expression was computed across all epithelial cells in the binned timepoints. Genes with a summed raw abundance <0.5 across all timepoints were filtered out. Genes with a log2 ratio of expression >1.5 between the before-injury timepoint and any healing timepoint were considered significant. The range of expression for each gene was normalized to between 0 and 1, and the temporal pattern of the gene set clustered using hierarchical clustering with an expected number of clusters, based on examination of the heatmap, set to 7. One cluster containing genes that peaked at the very-late timepoint was filtered out because it consisted primarily of squamous cell markers (e.g., *Krt14, Col17a1*) that were present in higher background abundance from the SNEC feature in the previously published dataset[34].

Gene lists were analyzed ontologically using enrichr[57]. The top 3 pathways with adjusted *P* value < 0.05 in each database were retained. Helper functions were written and collected in the R module "camMonocleHelper." These include functions for abundance calculations (e.g., aggregate_expression_by_factor()), plotting (e.g., plot_expression_with_dots() used for Fig. S5L), and pathway analysis (e.g., query_enrichr() used for Figs. 6B and 6G).

Re-analysis of human IBD single-cell RNA-Seq data—Data reported by Smillie et al.[42] were downloaded from the accession number SCP259 hosted at the Broad Institute Single-Cell Portal. Patients lacking paired inflamed and uninflamed samples were not included in downstream analyses. The expression matrix was incorporated as a CellDataSet object in monocle3. Batch correction between patients was performed using the align_cds() function in monocle3. Dimensional reduction and visualization were performed as for murine data collected in this study. Epithelial cells harboring significant expression of mesenchymal or myeloid markers upon leiden clustering were filtered out as potential doublets. The differential expression of each FPC conservative marker gene in each cluster was computed by subtracting the mean normalized expression value in the uninflamed sample from that of the inflamed sample.

Modeling of clonal distributions—Based on the qualitative findings, here we propose a minimal model of the clonal dynamics during repair. Taken together, the analysis of the changes in the anatomical organization combined with the clonal data suggests that repair proceeds through a process that has 2 basic phases (Fig. 3B). During the first phase (lateralization), ulcerated regions of the intestine are rapidly covered by a wound epithelium that derives from surviving epithelial cells. Here, crypts lose their structural integrity, becoming fused into a labyrinth-like network that extends into the injury-bed. This expansion is driven by a minority population of highly clonogenic cells – termed FPCs – that drive the coordinated expansion in a direction that correlates with the labyrinthine channels. Following re-epithelialization of the ulcerated regions, crypts then re-initiate within the channels to re-establish the characteristic glandular organization (morphogenesis), with evidence of residual crypt fission during this secondary process.

As the formation of a clonal field involves the lateral spread of a clone across the surface of the mucosa, thereby providing an anchor for new crypts, the dynamics of cell interactions during the initial lateralization phase will determine the overall field-forming potential of FPCs associated with wound repair. To gain insight into the dynamics of clonal expansion, we placed emphasis on the lognormal-like character of the clone size distribution (Figs. 3C and 4C). With the entire distribution dependent on just two parameters, the average and variance of the logarithm of clone size, such behavior suggests that the wide range of clone sizes may be captured within the framework of a minimal statistical model. Yet, the lognormal size dependence stands in stark contrast to the Gaussian- and exponential-like distributions that characterize clonal competition in one- and two-dimensional settings[58]. Typically, in the context of homeostatic turnover, clones evolve through a pattern of neutral cell dynamics based on competition for niche access: the loss of a renewing cell through differentiation is compensated by the division of neighbor to maintain constant the overall cell density. In the present case, clonal dynamics must be considered in a regenerative context in which the initial phase of re-epithelialization occurs through the directed expansion of a planar interface that spreads like a blanket across the ulcerated region. Nevertheless, local cell competition at the growing front would not be predicted to give rise to the lognormal-like clone size dependence observed here. So how can such a distribution arise?

Indeed, lognormal distributions may arise not through local cell competition but through local *cooperativity*. According to the central limit theorem, the distribution of sums of numbers drawn at random from a generic distribution converges rapidly towards a Gaussian dependence. By the same reasoning, it follows that the distribution of the products of positive random numbers are characterized by a lognormal dependence[59], a property known as Gibrat's law. If, during the re-epithelialization process, the symmetric duplication of FPCs and their progenies are locally correlated, clones will expand geometrically with the number of rounds of cell division. However, such dynamics are sustainable only if clones are not subject to steric constraints during their expansion, i.e., clones must be able to freely reposition during their expansion. Such behavior can occur if clones are able to spread efficiently as a liquid-like phase, as evidenced by the directed contiguous footprint of clones that orient towards the center of the ulcerated region. In this case, randomness enters not through the stochastic fate decision between individual cells – the decision to duplicate or differentiate – but through the total number of rounds of cell division that occur within a clone through the re-epithelialization process. This number may be influenced by several contributory factors including the timing of entry into the FPC-like state, the position of FPCs and their progenies with respect to the growing front, and local influences such as the degree of inflammation during the regenerative process.

At present, the empirical data do not permit us to differentiate between the strength of these different contributions, which can function in parallel. However, as a simple demonstration of these principles, we can formulate the number of doublings *m* for any given clone to be dependent on the duration of the wound healing process within the local environment (T), the time of initiation of cell division (T_0), and the time interval between cell divisions (τ):

$$m = \frac{T - T_0}{\tau}$$

From this relationship, if we assume that the variation in the wound healing duration (T) and the proliferative interval (τ) within a local environment is small (i.e., these parameters are set by larger tissue influences such as concentrations of cytokines, etc.), then the variance and shape of the clone-size distribution are determined by the variance and shape of the distribution of the initial time of reprogramming and cell division (T_0). In the case that T_0 are normally distributed, then the resulting clone-size distribution will be predicted to be log-normally distributed.

Finally, we note that, in this example, one can infer that the probability of reprogramming is dynamic, with a peak density occurring at a time point that is reflected by the mean of T_0. This compares favorably to estimates of the number of reprogrammed (Ly6a+) progenitor cells from the scRNA-seq data – the number of reprogrammed proliferative progenitors rises and falls around a peak during middle healing (Fig. 5K).

We performed a heuristic evaluation of the differences that arise in the clone-size distribution between competitive (i.e., constrained) and coordinated models of stem cell proliferation. The goal of these simulations was not to provide absolute fits to the experimental data, but rather to demonstrate the differences in fundamental forms derived

from these distinct types of cellular dynamics. To establish a competitive simulation, we constructed a regenerative compartment containing 100 proliferation-competent cells. The compartment was constrained to grow at a constant rate of 1 cell/turn, which was enforced by randomly choosing 1 cell in the compartment for division. The simulation ended once the total size of the compartment exceeded 1,000x the initial size. The resulting clone sizes were aggregated from 20 trials and fit to different distributions using the fitdistrplus package in R. The results are shown in Fig. 4E-G.

The coordinated simulation was constructed with similar initial conditions (100 proliferation-competent cells). The cells were assigned an individual proliferation frequency chosen from a normal distribution, such that the mean interval of proliferation across the cells was 50 turns. For a given cell lineage, each proliferative event resulted in a doubling of the lineage. The simulation was terminated once the summed size of all lineages was 1,000x the initial compartment size. The simulation was repeated for 50 trials. The results are shown in Fig. 4H-J and are a good fit to a lognormal distribution.

Whole exome sequencing—Reads were aligned to the mouse genome (mm10) using bowtie2 2.3.5.1[60] (http://bowtie-bio.sourceforge.net/bowtie2/index.shtml). SAM files were converted to BAM files and sorted using Samtools (http://www.htslib.org/). Variant call files were produced using the "mpileup" feature of Bcftools[61] (http://samtools.github.io/bcftools/bcftools.html) with a maximum depth parameter of 8000. The variants were filtered using the "filter" command of Bcftools, with the filtering parameters set to QUAL >= 100, IndelGap =10, SnpGap = 3. The number of SNPs and indels was computed as a function of the average read depth per animal. The variants unique to DSS and AOM/DSS-treated samples were identified by filtering out the intersection of variants with the water-treated samples, using the "isec" command of Bcftools. Protein-coding variants were identified and annotated using the UCSC Variant Annotation Integrator (https://genome.ucsc.edu/cgi-bin/hgVai).

Supplementary Material

Refer to Web version on PubMed Central for supplementary material.

Acknowledgments / Funding

Inclusion and Diversity

We support inclusive, diverse, and equitable conduct of research.

References

1. Kim ER, and Chang DK (2014). Colorectal cancer in inflammatory bowel disease: the risk, pathogenesis, prevention and diagnosis. World J Gastroenterol 20, 9872–9881. 10.3748/wjg.v20.i29.9872. [PubMed: 25110418]

2. Braakhuis BJ, Tabor MP, Kummer JA, Leemans CR, and Brakenhoff RH (2003). A genetic explanation of Slaughter's concept of field cancerization: evidence and clinical implications. Cancer Res 63, 1727–1730. [PubMed: 12702551]

3. Slaughter DP, Southwick HW, and Smejkal W (1953). Field cancerization in oral stratified squamous epithelium; clinical implications of multicentric origin. Cancer 6, 963–968. 10.1002/1097-0142(195309)6:5<963::aid-cncr2820060515>3.0.co;2-q. [PubMed: 13094644]

4. Yum MK, Han S, Fink J, Wu SS, Dabrowska C, Trendafilova T, Mustata R, Chatzeli L, Azzarelli R, Pshenichnaya I, et al. (2021). Tracing oncogene-driven remodelling of the intestinal stem cell niche. Nature 594, 442–447. 10.1038/s41586-021-03605-0. [PubMed: 34079126]

5. Snippert HJ, Schepers AG, van Es JH, Simons BD, and Clevers H (2014). Biased competition between Lgr5 intestinal stem cells driven by oncogenic mutation induces clonal expansion. EMBO Rep 15, 62–69. 10.1002/embr.201337799. [PubMed: 24355609]

6. van Neerven SM, de Groot NE, Nijman LE, Scicluna BP, van Driel MS, Lecca MC, Warmerdam DO, Kakkar V, Moreno LF, Vieira Braga FA, et al. (2021). Apc-mutant cells act as supercompetitors in intestinal tumour initiation. Nature 594, 436–441. 10.1038/s41586-021-03558-4. [PubMed: 34079128]

7. Flanagan DJ, Pentinmikko N, Luopajarvi K, Willis NJ, Gilroy K, Raven AP, McGarry L, Englund JI, Webb AT, Scharaw S, et al. (2021). NOTUM from Apc-mutant cells biases clonal competition to initiate cancer. Nature 594, 430–435. 10.1038/s41586-021-03525-z. [PubMed: 34079124]

8. Vermeulen L, Morrissey E, van der Heijden M, Nicholson AM, Sottoriva A, Buczacki S, Kemp R, Tavare S, and Winton DJ (2013). Defining stem cell dynamics in models of intestinal tumor initiation. Science 342, 995–998. 10.1126/science.1243148. [PubMed: 24264992]

9. Nanki K, Fujii M, Shimokawa M, Matano M, Nishikori S, Date S, Takano A, Toshimitsu K, Ohta Y, Takahashi S, et al. (2020). Somatic inflammatory gene mutations in human ulcerative colitis epithelium. Nature 577, 254–259. 10.1038/s41586-019-1844-5. [PubMed: 31853059]

10. Kakiuchi N, Yoshida K, Uchino M, Kihara T, Akaki K, Inoue Y, Kawada K, Nagayama S, Yokoyama A, Yamamoto S, et al. (2020). Frequent mutations that converge on the NFKBIZ pathway in ulcerative colitis. Nature 577, 260–265. 10.1038/s41586-019-1856-1. [PubMed: 31853061]

11. Olafsson S, McIntyre RE, Coorens T, Butler T, Jung H, Robinson PS, Lee-Six H, Sanders MA, Arestang K, Dawson C, et al. (2020). Somatic Evolution in Non-neoplastic IBD-Affected Colon. Cell 182, 672–684 e611. 10.1016/j.cell.2020.06.036. [PubMed: 32697969]

12. Kakiuchi N, and Ogawa S (2021). Clonal expansion in non-cancer tissues. Nat Rev Cancer 21, 239–256. 10.1038/s41568-021-00335-3. [PubMed: 33627798]

13. Leedham SJ, Graham TA, Oukrif D, McDonald SA, Rodriguez-Justo M, Harrison RF, Shepherd NA, Novelli MR, Jankowski JA, and Wright NA (2009). Clonality, founder mutations, and field cancerization in human ulcerative colitis-associated neoplasia. Gastroenterology 136, 542–550 e546. 10.1053/j.gastro.2008.10.086. [PubMed: 19103203]

14. Lyda MH, Noffsinger A, Belli J, Fischer J, and Fenoglio-Preiser CM (1998). Multifocal neoplasia involving the colon and appendix in ulcerative colitis: pathological and molecular features. Gastroenterology 115, 1566–1573. 10.1016/s0016-5085(98)70037-x. [PubMed: 9834286]

15. Salk JJ, Salipante SJ, Risques RA, Crispin DA, Li L, Bronner MP, Brentnall TA, Rabinovitch PS, Horwitz MS, and Loeb LA (2009). Clonal expansions in ulcerative colitis identify patients with neoplasia. Proc Natl Acad Sci U S A 106, 20871–20876. 10.1073/pnas.0909428106. [PubMed: 19926851]

16. Galandiuk S, Rodriguez-Justo M, Jeffery R, Nicholson AM, Cheng Y, Oukrif D, Elia G, Leedham SJ, McDonald SA, Wright NA, and Graham TA (2012). Field cancerization in the intestinal epithelium of patients with Crohn's ileocolitis. Gastroenterology 142, 855–864 e858. 10.1053/j.gastro.2011.12.004. [PubMed: 22178590]

17. Liu CY, Cham CM, and Chang EB (2021). Epithelial wound healing in inflammatory bowel diseases: the next therapeutic frontier. Transl Res. 10.1016/j.trsl.2021.06.001.

18. Miyoshi H, Ajima R, Luo CT, Yamaguchi TP, and Stappenbeck TS (2012). Wnt5a potentiates TGF-beta signaling to promote colonic crypt regeneration after tissue injury. Science 338, 108–113. 10.1126/science.1223821. [PubMed: 22956684]

19. Seno H, Miyoshi H, Brown SL, Geske MJ, Colonna M, and Stappenbeck TS (2009). Efficient colonic mucosal wound repair requires Trem2 signaling. Proc Natl Acad Sci U S A 106, 256–261. 10.1073/pnas.0803343106. [PubMed: 19109436]

20. Murata K, Jadhav U, Madha S, van Es J, Dean J, Cavazza A, Wucherpfennig K, Michor F, Clevers H, and Shivdasani RA (2020). Ascl2-Dependent Cell Dedifferentiation Drives Regeneration of Ablated Intestinal Stem Cells. Cell Stem Cell 26, 377–390 e376. 10.1016/j.stem.2019.12.011. [PubMed: 32084390]

21. Tetteh PW, Basak O, Farin HF, Wiebrands K, Kretzschmar K, Begthel H, van den Born M, Korving J, de Sauvage F, van Es JH, et al. (2016). Replacement of Lost Lgr5-Positive Stem Cells through Plasticity of Their Enterocyte-Lineage Daughters. Cell Stem Cell 18, 203–213. 10.1016/j.stem.2016.01.001. [PubMed: 26831517]

22. Sangiorgi E, and Capecchi MR (2008). Bmi1 is expressed in vivo in intestinal stem cells. Nat Genet 40, 915–920. 10.1038/ng.165. [PubMed: 18536716]

23. Tian H, Biehs B, Warming S, Leong KG, Rangell L, Klein OD, and de Sauvage FJ (2011). A reserve stem cell population in small intestine renders Lgr5-positive cells dispensable. Nature 478, 255–259. 10.1038/nature10408. [PubMed: 21927002]

24. Wang Y, Chiang IL, Ohara TE, Fujii S, Cheng J, Muegge BD, Ver Heul A, Han ND, Lu Q, Xiong S, et al. (2019). Long-Term Culture Captures Injury-Repair Cycles of Colonic Stem Cells. Cell 179, 1144–1159 e1115. 10.1016/j.cell.2019.10.015. [PubMed: 31708126]

25. Ayyaz A, Kumar S, Sangiorgi B, Ghoshal B, Gosio J, Ouladan S, Fink M, Barutcu S, Trcka D, Shen J, et al. (2019). Single-cell transcriptomes of the regenerating intestine reveal a revival stem cell. Nature 569, 121–125. 10.1038/s41586-019-1154-y. [PubMed: 31019301]

26. Nusse YM, Savage AK, Marangoni P, Rosendahl-Huber AKM, Landman TA, de Sauvage FJ, Locksley RM, and Klein OD (2018). Parasitic helminths induce fetal-like reversion in the intestinal stem cell niche. Nature 559, 109–113. 10.1038/s41586-018-0257-1. [PubMed: 29950724]

27. Yui S, Azzolin L, Maimets M, Pedersen MT, Fordham RP, Hansen SL, Larsen HL, Guiu J, Alves MRP, Rundsten CF, et al. (2018). YAP/TAZ-Dependent Reprogramming of Colonic Epithelium Links ECM Remodeling to Tissue Regeneration. Cell Stem Cell 22, 35–49 e37. 10.1016/j.stem.2017.11.001. [PubMed: 29249464]

28. Liu CY, and Polk DB (2020). Cellular maps of gastrointestinal organs: getting the most from tissue clearing. Am J Physiol Gastrointest Liver Physiol 319, G1–G10. 10.1152/ajpgi.00075.2020. [PubMed: 32421359]

29. Liu CY, Dube PE, Girish N, Reddy AT, and Polk DB (2015). Optical reconstruction of murine colorectal mucosa at cellular resolution. Am J Physiol Gastrointest Liver Physiol 308, G721–735. 10.1152/ajpgi.00310.2014. [PubMed: 25721303]

30. DeRoche TC, Xiao SY, and Liu X (2014). Histological evaluation in ulcerative colitis. Gastroenterol Rep (Oxf) 2, 178–192. 10.1093/gastro/gou031. [PubMed: 24942757]

31. Kozar S, Morrissey E, Nicholson AM, van der Heijden M, Zecchini HI, Kemp R, Tavare S, Vermeulen L, and Winton DJ (2013). Continuous clonal labeling reveals small numbers of functional stem cells in intestinal crypts and adenomas. Cell Stem Cell 13, 626–633. 10.1016/j.stem.2013.08.001. [PubMed: 24035355]

32. Lopez-Garcia C, Klein AM, Simons BD, and Winton DJ (2010). Intestinal stem cell replacement follows a pattern of neutral drift. Science 330, 822–825. 10.1126/science.1196236. [PubMed: 20929733]

33. Snippert HJ, van der Flier LG, Sato T, van Es JH, van den Born M, Kroon-Veenboer C, Barker N, Klein AM, van Rheenen J, Simons BD, and Clevers H (2010). Intestinal crypt homeostasis results from neutral competition between symmetrically dividing Lgr5 stem cells. Cell 143, 134–144. 10.1016/j.cell.2010.09.016. [PubMed: 20887898]

34. Liu CY, Girish N, Gomez ML, Dube PE, Washington MK, Simons BD, and Polk DB (2022). Transitional Anal Cells Mediate Colonic Re-epithelialization in Colitis. Gastroenterology 162, 1975–1989. 10.1053/j.gastro.2022.02.031. [PubMed: 35227778]

35. Hopkins AM, Pineda AA, Winfree LM, Brown GT, Laukoetter MG, and Nusrat A (2007). Organized migration of epithelial cells requires control of adhesion and protrusion through Rho kinase effectors. Am J Physiol Gastrointest Liver Physiol 292, G806–817. 10.1152/ajpgi.00333.2006. [PubMed: 17138966]

36. Beck PL, Rosenberg IM, Xavier RJ, Koh T, Wong JF, and Podolsky DK (2003). Transforming growth factor-beta mediates intestinal healing and susceptibility to injury in vitro and in vivo through epithelial cells. Am J Pathol 162, 597–608. 10.1016/s0002-9440(10)63853-9. [PubMed: 12547717]

37. Dignass AU, and Podolsky DK (1993). Cytokine modulation of intestinal epithelial cell restitution: central role of transforming growth factor beta. Gastroenterology 105, 1323–1332. 10.1016/0016-5085(93)90136-z. [PubMed: 8224636]

38. Girish N, Liu CY, Gadeock S, Gomez ML, Huang Y, Sharifkhodaei Z, Washington MK, and Polk DB (2021). Persistence of Lgr5+ colonic epithelial stem cells in mouse models of inflammatory bowel disease. Am J Physiol Gastrointest Liver Physiol. 10.1152/ajpgi.00248.2020.

39. Mustata RC, Vasile G, Fernandez-Vallone V, Strollo S, Lefort A, Libert F, Monteyne D, Perez-Morga D, Vassart G, and Garcia MI (2013). Identification of Lgr5-independent spheroid-generating progenitors of the mouse fetal intestinal epithelium. Cell Rep 5, 421–432. 10.1016/j.celrep.2013.09.005. [PubMed: 24139799]

40. Metcalfe C, Kljavin NM, Ybarra R, and de Sauvage FJ (2014). Lgr5+ stem cells are indispensable for radiation-induced intestinal regeneration. Cell Stem Cell 14, 149–159. 10.1016/j.stem.2013.11.008. [PubMed: 24332836]

41. Serra D, Mayr U, Boni A, Lukonin I, Rempfler M, Challet Meylan L, Stadler MB, Strnad P, Papasaikas P, Vischi D, et al. (2019). Self-organization and symmetry breaking in intestinal organoid development. Nature 569, 66–72. 10.1038/s41586-019-1146-y. [PubMed: 31019299]

42. Smillie CS, Biton M, Ordovas-Montanes J, Sullivan KM, Burgin G, Graham DB, Herbst RH, Rogel N, Slyper M, Waldman J, et al. (2019). Intra- and Inter-cellular Rewiring of the Human Colon during Ulcerative Colitis. Cell 178, 714–730 e722. 10.1016/j.cell.2019.06.029. [PubMed: 31348891]

43. Davidson LA, Goldsby JS, Callaway ES, Shah MS, Barker N, and Chapkin RS (2012). Alteration of colonic stem cell gene signatures during the regenerative response to injury. Biochim Biophys Acta 1822, 1600–1607. 10.1016/j.bbadis.2012.06.011. [PubMed: 22750333]

44. Powell AE, Wang Y, Li Y, Poulin EJ, Means AL, Washington MK, Higginbotham JN, Juchheim A, Prasad N, Levy SE, et al. (2012). The pan-ErbB negative regulator Lrig1 is an intestinal stem cell marker that functions as a tumor suppressor. Cell 149, 146–158. 10.1016/j.cell.2012.02.042. [PubMed: 22464327]

45. Jiang M, Li H, Zhang Y, Yang Y, Lu R, Liu K, Lin S, Lan X, Wang H, Wu H, et al. (2017). Transitional basal cells at the squamous-columnar junction generate Barrett's oesophagus. Nature 550, 529–533. 10.1038/nature24269. [PubMed: 29019984]

46. McElrath C, Espinosa V, Lin JD, Peng J, Sridhar R, Dutta O, Tseng HC, Smirnov SV, Risman H, Sandoval MJ, et al. (2021). Critical role of interferons in gastrointestinal injury repair. Nat Commun 12, 2624. 10.1038/s41467-021-22928-0. [PubMed: 33976143]

47. Ohara TE, Colonna M, and Stappenbeck TS (2022). Adaptive differentiation promotes intestinal villus recovery. Dev Cell 57, 166–179 e166. 10.1016/j.devcel.2021.12.012. [PubMed: 35016013]

48. Liu CY, Polk DB, and Frey MR (2018). Mucosal Restitution and Repair. In Physiology of the Gastrointestinal Tract (Sixth Edition), Said HM, ed. (Academic Press), pp. 683–708.

49. Shivdasani RA, Clevers H, and de Sauvage FJ (2021). Tissue regeneration: Reserve or reverse? Science 371, 784–786. 10.1126/science.abb6848. [PubMed: 33602845]

50. Liu CY, Tam SS, Huang Y, Dube PE, Alhosh R, Girish N, Punit S, Nataneli S, Li F, Bender JM, et al. (2020). TNF Receptor 1 Promotes Early-Life Immunity and Protects against Colitis in Mice. Cell Rep 33, 108275. 10.1016/j.celrep.2020.108275. [PubMed: 33086075]

51. Dube PE, Liu CY, Girish N, Washington MK, and Polk DB (2018). Pharmacological activation of epidermal growth factor receptor signaling inhibits colitis-associated cancer in mice. Sci Rep 8, 9119. 10.1038/s41598-018-27353-w. [PubMed: 29904166]

52. Renier N, Wu Z, Simon DJ, Yang J, Ariel P, and Tessier-Lavigne M (2014). iDISCO: a simple, rapid method to immunolabel large tissue samples for volume imaging. Cell 159, 896–910. 10.1016/j.cell.2014.10.010. [PubMed: 25417164]

53. Liu CY, Xiao C, Fraser SE, Lester HA, and Koos DS (2012). Electrophysiological characterization of Grueneberg ganglion olfactory neurons: spontaneous firing, sodium conductance, and hyperpolarization-activated currents. J Neurophysiol 108, 1318–1334. 10.1152/jn.00907.2011. [PubMed: 22649209]

54. Cao J, Spielmann M, Qiu X, Huang X, Ibrahim DM, Hill AJ, Zhang F, Mundlos S, Christiansen L, Steemers FJ, et al. (2019). The single-cell transcriptional landscape of mammalian organogenesis. Nature 566, 496–502. 10.1038/s41586-019-0969-x. [PubMed: 30787437]

55. Haghverdi L, Lun ATL, Morgan MD, and Marioni JC (2018). Batch effects in single-cell RNA-sequencing data are corrected by matching mutual nearest neighbors. Nat Biotechnol 36, 421–427. 10.1038/nbt.4091. [PubMed: 29608177]

56. Heng TS, Painter MW, and Immunological Genome Project C (2008). The Immunological Genome Project: networks of gene expression in immune cells. Nat Immunol 9, 1091–1094. 10.1038/ni1008-1091. [PubMed: 18800157]

57. Chen EY, Tan CM, Kou Y, Duan Q, Wang Z, Meirelles GV, Clark NR, and Ma'ayan A (2013). Enrichr: interactive and collaborative HTML5 gene list enrichment analysis tool. BMC Bioinformatics 14, 128. 10.1186/1471-2105-14-128. [PubMed: 23586463]

58. Klein AM, and Simons BD (2011). Universal patterns of stem cell fate in cycling adult tissues. Development 138, 3103–3111. 10.1242/dev.060103. [PubMed: 21750026]

59. Huxley JS (1932). Problems of relative growth.

60. Langmead B, and Salzberg SL (2012). Fast gapped-read alignment with Bowtie 2. Nat Methods 9, 357–359. 10.1038/nmeth.1923. [PubMed: 22388286]

61. Li H. (2011). A statistical framework for SNP calling, mutation discovery, association mapping and population genetical parameter estimation from sequencing data. Bioinformatics 27, 2987–2993. 10.1093/bioinformatics/btr509. [PubMed: 21903627]

62. Madisen L, Zwingman TA, Sunkin SM, Oh SW, Zariwala HA, Gu H, Ng LL, Palmiter RD, Hawrylycz MJ, Jones AR, et al. (2010). A robust and high-throughput Cre reporting and characterization system for the whole mouse brain. Nat Neurosci 13, 133–140. 10.1038/nn.2467. [PubMed: 20023653]

63. Muzumdar MD, Tasic B, Miyamichi K, Li L, and Luo L (2007). A global double-fluorescent Cre reporter mouse. Genesis 45, 593–605. 10.1002/dvg.20335. [PubMed: 17868096]

64. el Marjou F, Janssen KP, Chang BH, Li M, Hindie V, Chan L, Louvard D, Chambon P, Metzger D, and Robine S (2004). Tissue-specific and inducible Cre-mediated recombination in the gut epithelium. Genesis 39, 186–193. 10.1002/gene.20042. [PubMed: 15282745]

65. Barker N, van Es JH, Kuipers J, Kujala P, van den Born M, Cozijnsen M, Haegebarth A, Korving J, Begthel H, Peters PJ, and Clevers H (2007). Identification of stem cells in small intestine and colon by marker gene Lgr5. Nature 449, 1003–1007. 10.1038/nature06196. [PubMed: 17934449]

66. McMahon AP, Aronow BJ, Davidson DR, Davies JA, Gaido KW, Grimmond S, Lessard JL, Little MH, Potter SS, Wilder EL, et al. (2008). GUDMAP: the genitourinary developmental molecular anatomy project. J Am Soc Nephrol 19, 667–671. 10.1681/ASN.2007101078. [PubMed: 18287559]

67. Subramanian A, Tamayo P, Mootha VK, Mukherjee S, Ebert BL, Gillette MA, Paulovich A, Pomeroy SL, Golub TR, Lander ES, and Mesirov JP (2005). Gene set enrichment analysis: a knowledge-based approach for interpreting genome-wide expression profiles. Proc Natl Acad Sci U S A 102, 15545–15550. 10.1073/pnas.0506580102. [PubMed: 16199517]

68. Schindelin J, Arganda-Carreras I, Frise E, Kaynig V, Longair M, Pietzsch T, Preibisch S, Rueden C, Saalfeld S, Schmid B, et al. (2012). Fiji: an open-source platform for biological-image analysis. Nat Methods 9, 676–682. 10.1038/nmeth.2019. [PubMed: 22743772]

69. Li H, Handsaker B, Wysoker A, Fennell T, Ruan J, Homer N, Marth G, Abecasis G, Durbin R, and Genome Project Data Processing, S. (2009). The Sequence Alignment/Map format and SAMtools. Bioinformatics 25, 2078–2079. 10.1093/bioinformatics/btp352. [PubMed: 19505943]

Highlights

- Epithelial healing in colitis massively clones founder progenitor cells (FPCs).

- Healing is a fluidic epithelial spreading process across loosened crypt boundaries.

- FPCs emerge from regeneratively reprogrammed epithelium.

- Wound healing represents a temporary period of crypt and lineage plasticity.
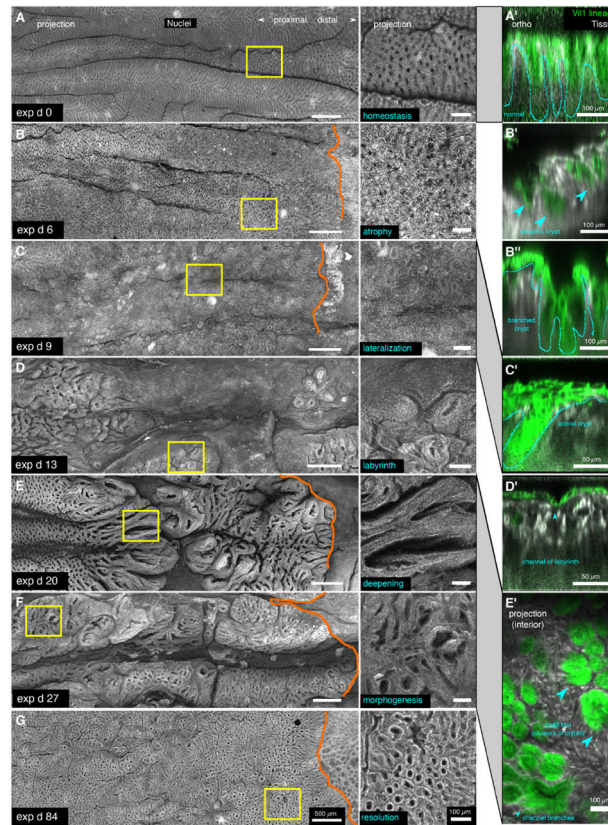
Figure 1: Sequential remodeling of epithelium during acute colitis.

Vil1::Cre;*Rosa26*::mTmG ("Vil1-mTmG") mice (n 4 per timepoint) express membrane-bound GFP in cells of intestinal epithelial lineage. Mice were exposed to 3% DSS for 6 d, beginning on experimental day (exp d) 0, to induce distal colonic injury and inflammation. Distal colons were isolated and stained with methyl green to reveal cellular nuclei. Whole-mount microscopy of chemically cleared specimens revealed the 3d cellular arrangements of the tissue in z-projections (left panels) and superimposed epithelial lineages in orthogonal rotations (rightmost prime panels). Yellow boxes indicate areas of magnification shown in the center panels. The orange line denotes the squamocolumnar junction separating intestinal from anal-derived tissue. A) Normal colon (exp d 0) is a repetitive array of crypts. B) Early epithelial responses to injury (exp d 6) include atrophy and crypt branching. C) Gross epithelial cell loss (exp d 9) is associated with a side-lying crypt structure. D) Early morphogenesis (exp d 13) involves the appearance of shallow surface invaginations linked together in a labyrinth. E) Over time (exp d 20), these invaginations deepen. F) At a later recovery timepoint (exp d 27), the base of the invaginations harbors clusters of crypts connected in a branched structure (foci). G) Gross recovery is observed by exp d 84.
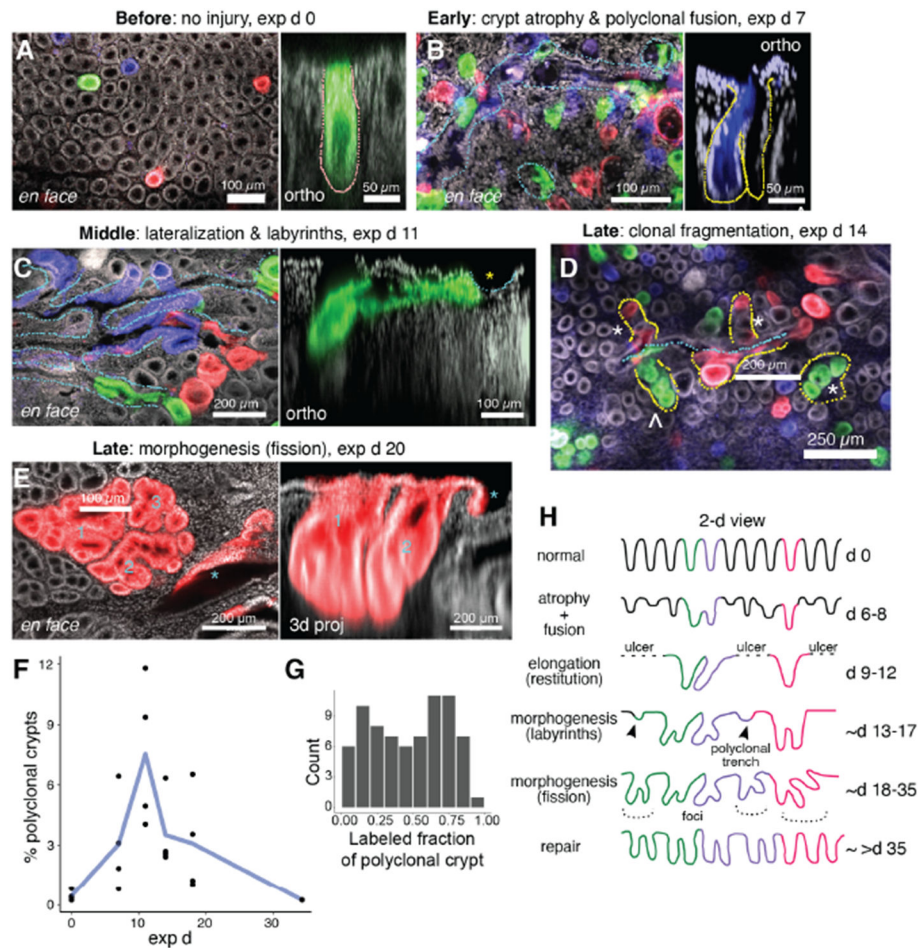
Figure 2: Crypt lineages mix and re-compartmentalize during mucosal healing.
Vil1::CreER;*Rosa26*::Confetti ("Vil1-Confetti") mice were injected with 1 mg tamoxifen 12 wks prior to a 6-day exposure to 3% DSS. The tissue was chemically cleared to induce optical transparency and to reveal whole crypts labeled in a mosaic fashion. Fluorophores have been false-colored as blue (membrane CFP), green (cytosolic YFP), red (cytosolic RFP), and white (nuclear methyl green dye) to facilitate visualization. Nuclear GFP signal was not recovered in significant amounts but could be theoretically separated from YFP by its differential nuclear vs. cytosolic localization. High-resolution imaging facilitated analysis of fundamental forms of crypts associated with healing (n ≥ 3 mice per timepoint). *En face* images show the lateral extent and mixing of crypt-derived cells. Orthogonal reconstructions and 3d projections (of a different color patch than is shown in *en face* images) demonstrate the view of crypt morphology from the classic histological plane. Timepoints of healing are broadly classified as early, middle, and late, with further definition in quantitative analyses and transcriptomic studies. A) Fully labeled crypts are found prior to injury. B) After withdrawal of DSS, crypts undergo fusion with neighbors (yellow dotted lines) to form polyclonal networks (blue dotted lines). C) The formation of the labyrinth of invaginations (blue dotted lines) involves multiple crypts of distinct lineage. In the orthogonal projection, shown is a crypt partially contributing to a new invagination (asterisk). D) The combination of mixing and early re-compartmentalization (new crypt

formation) irrespective of clonal boundary results in apparent clonal fragmentation (yellow dotted lines) and sporadic findings of crypt polyclonality (asterisks) next to monoclonal crypts (^) along the labyrinthine invaginations (blue dotted lines). E) Later stages of healing are characterized by crypt fission within numbered foci that are located asymmetrically in the color patch (asterisk denotes residual invagination). F) The fraction of polyclonal crypts was elevated at exp d 9-13 (middle healing), approximately the initiation of crypt morphogenesis. G) Examination of these polyclonal crypts (n=7 mice) reveals an even distribution of labeling, consistent with crypt morphogenesis proceeding irrespective of clonal boundary. H) The diagram summarizes the overall model of crypt-level changes during repair.
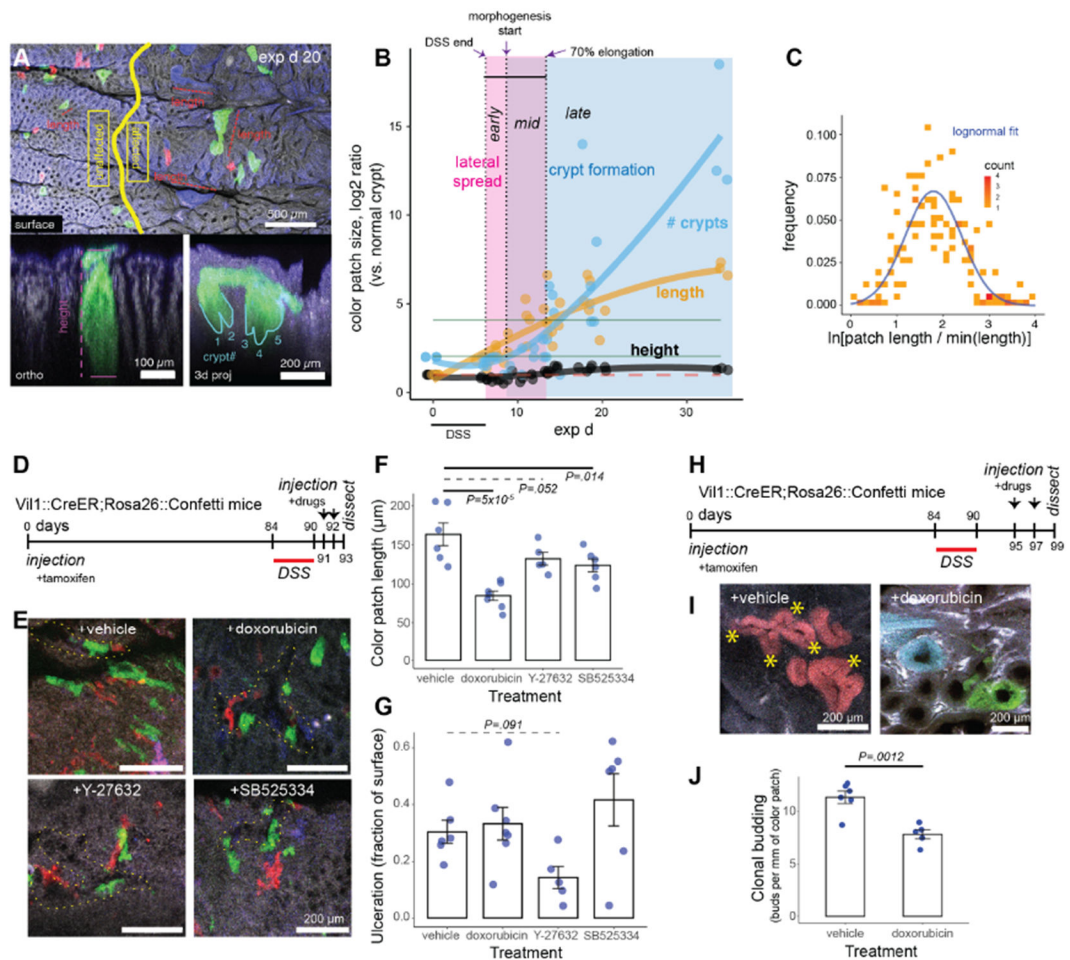
Figure 3: Epithelial repair proceeds through partially overlapping phases of crypt elongation and budding.

A) From the data presented in Fig. 2, the height, length, and crypt multiplicity (number of crypts) per color patch were quantified in the injured ("affected") colonic region and normalized to the neighboring proximal "unaffected" region. B) Shown are these values for the "leading" set of the 10 largest color patches per animal. Each point represents the median leading value for each animal. The plot demonstrates an early phase where color patches grow laterally (elongation) followed by a phase of crypt fission (formation/ morphogenesis). These partially overlapping phases are categorized as early, middle, and late healing. C) Color patch lengths obtained from the full population in the affected region form a lognormal distribution (n=3 mice). D-G) Short-term treatment with pharmacological inhibitors (20 mg/kg, i.p.) of proliferation (doxorubicin), ROCK (Y-27632, migration), or TGFβ receptor 1 (SB525334) during early healing (D) results in reduced crypt lateral spread (E,F), with the strongest effect seen with doxorubicin. Evidence of merging crypt structures (outlined with dotted yellow line) persisted with all treatments. The effect of Y-27632 may have been partially due to a weak effect on the restriction of injury, which limited the overall potential spread (G). H-J) Treatment with doxorubicin during middle/late healing tested the role of mitotic signaling on crypt budding (H). Asterisks denote example buds. Doxorubicin

reduced the number of crypt buds that formed within the depth of the labyrinth (I,J). Error bars: SEM. Significance test: pairwise t-tests with false discovery rate correction.
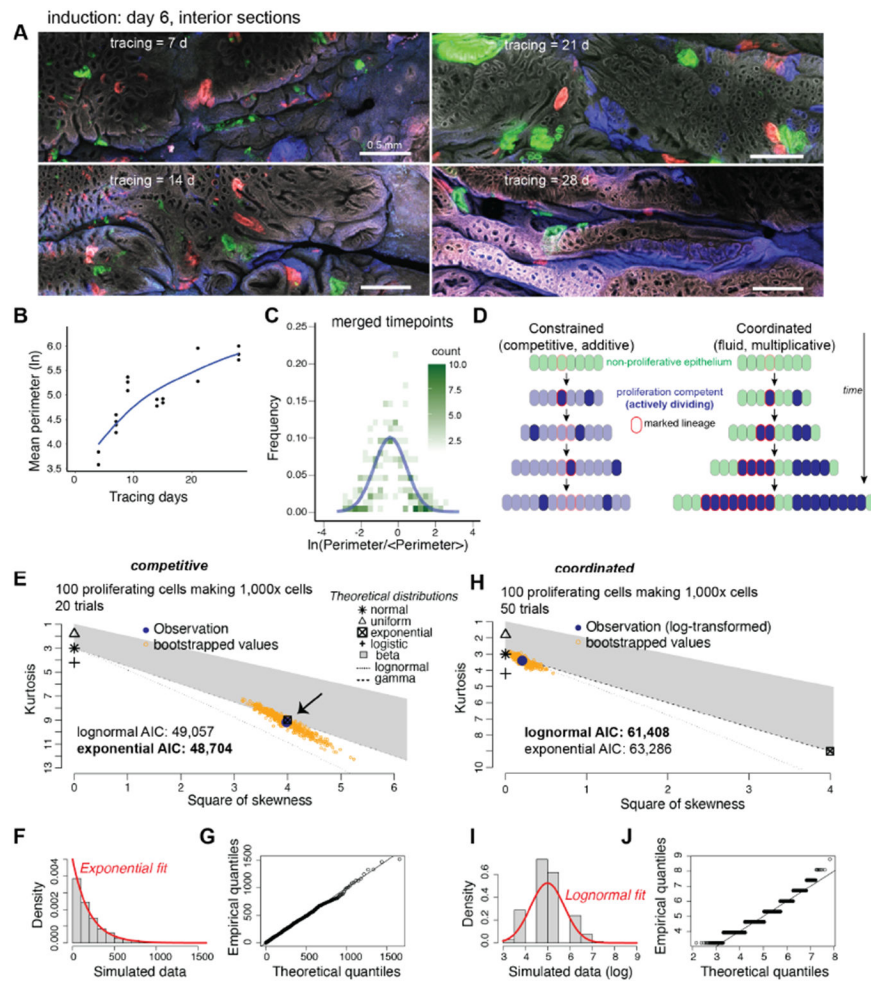
Figure 4: Statistical principles govern rapid establishment of clonal fields from founder progenitor cells.

Tracing was initiated at exp d 6, at the end of the 6-day DSS treatment. A) Images from interior z-projections of the colon show the growth of color patches into monoclonal fields over time (n 3 mice per timepoint). B) The plot shows the growth of the color patch perimeters over time. C) The unbiased distribution of color patch perimeters (40-60 patches/animal) follows an approximate lognormal distribution. The distribution is simplified by merging all tracing timepoints and dividing the perimeter values by the mean perimeter. D) The diagram illustrates two competing modes of clonal growth. In the competitive/constrained mode, all cells are competent for proliferation, but the rate of proliferation is fixed such that daughter cells compete to gain cells at each time period. The resulting clones grow at a rate proportional to their size. In the coordinated/less-constrained mode, a subset of cells commits to a distinct proliferative fate, and their lineages double at each time period. E-G) Predicted statistical distribution of clone sizes from simulations of the competitive model, in which 100 proliferative cells must regenerate a region of 1,000x size. The Cullen and Frey graph shows the simulated values to have a skewness and kurtosis consistent with exponentially distributed data (E), with a better Akaike information criterion (AIC) for exponential vs. lognormal fitting. The exponential probability density

(F) and quantile-quantile plot (G) support a qualitatively good fit to the simulation data. H-J) Similar simulations of clone size performed with the coordinated model, with the log-transformed data showing a good fit to the normal distribution on the Cullen and Frey graph (H), and with the raw data well-estimated by a lognormal density (I) and quantile-quantile assessment (J). These simulations support that the empirical distributions arise from coordinated behaviors of progenitor cell lineages.
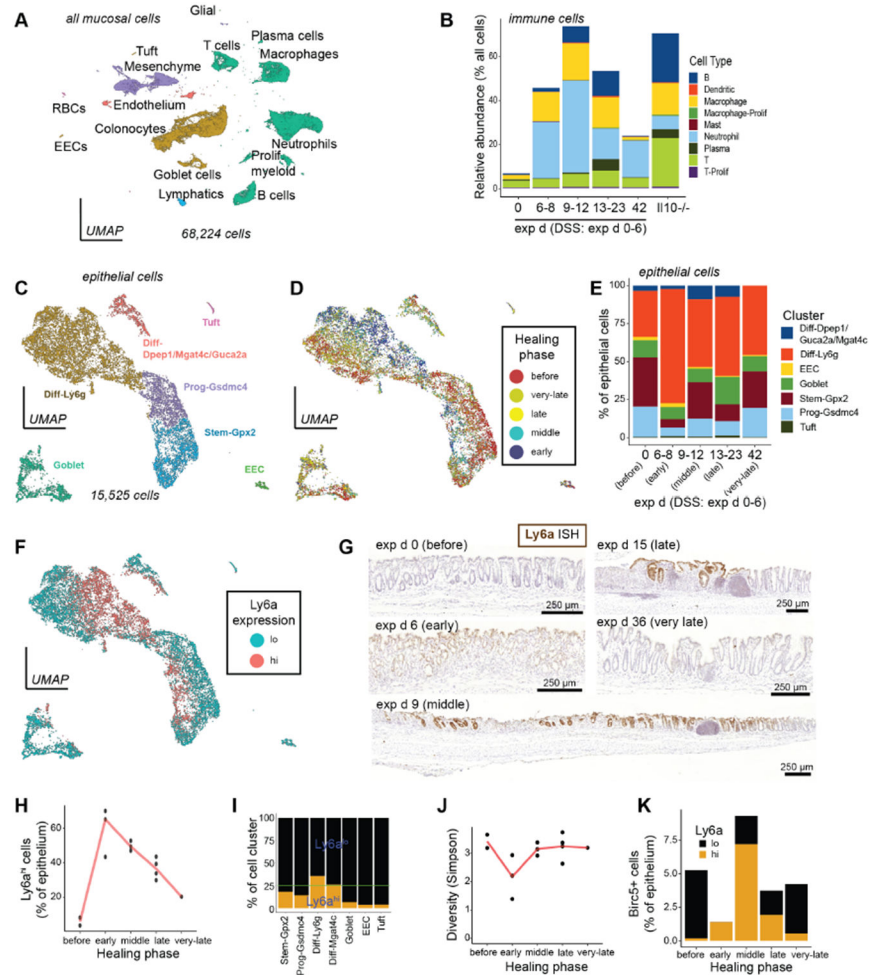
Figure 5: Proliferative FPC lineages emerge from Ly6a^hi epithelium during early healing.
Colonic mucosae from uninjured (exp d 0, D0 or "before"), DSS-treated (exp d 6-42), and
Il10^−/− (IL10) mice (n=3-8 mice merged per library) were dissociated and analyzed using
10X Chromium single-cell RNA-Seq. Libraries from DSS-treated mice were combined
to represent early (exp d 6-8), middle (exp d 9-12), late (exp d 13-23), or very-late
(exp d 42) healing timepoints for consistency with imaging studies and for increased
statistical power. A) As shown in the UMAP, samples were merged, and cells clustered,
to define distinct epithelial and stromal cell types. B) Analysis of immune cells shows
increased infiltration during DSS-induced and *Il10^−/−* injury, but with a higher proportion
of myeloid cells in DSS injury and lymphocytes in *Il10^−/−* injury. C) Subclustering of
epithelial cells defines clusters of stem (Stem-*Gpx2*) and undifferentiated (Prog-*Gsdmc4*)
cells, along with groups of absorptive (Diff) and secretory (Goblet, Tuft, enteroendocrine
(EEC)) cells. D) Color-coding the UMAP by healing stage shows reversible global changes
in single-cell transcriptomes from early healing to resolution. E) Stacked bar plot of
epithelial cell abundance demonstrates relative expansion of differentiated cells during
early healing. F-G) Epithelial cells could be gated by *Ly6a* expression (F), which defined
crypts undergoing active remodeling within the wound (G). H) Proportion of *Ly6a^hi* cells
peaks during early healing and gradually declines. I) *Ly6a^hi* cells are relatively depleted of

secretory lineages. The green line indicates the expected fraction of cells based on overall *Ly6a*^{hi} cell abundance. J) The relative expansion of *Ly6a*^{hi} differentiated cells during early healing contributes to reduced epithelial cell diversity. K) Proliferating (i.e., *Birc5+*) cells are reduced during early healing but are exclusively *Ly6a*^{hi}, supporting initiation of FPC lineages from this population.
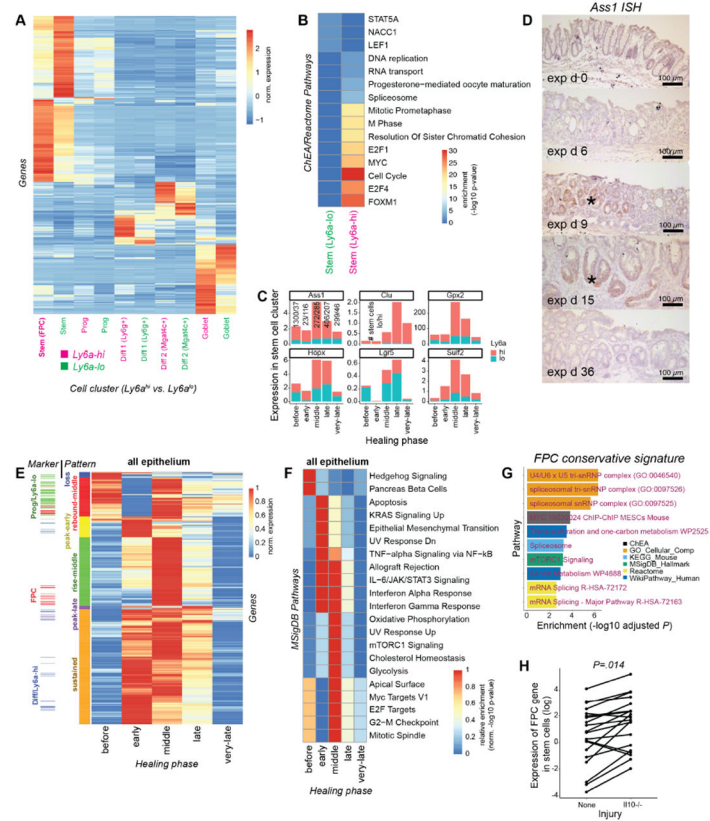
Figure 6: FPCs are a powerfully proliferative population defined by enriched metabolic signaling and activated spliceosomal pathways.

A) The heatmap demonstrates identification of gene markers of *Ly6a*^{hi} vs. *Ly6a*^{lo} epithelial cell clusters. B) Markers of the *Ly6a*^{hi} stem cell cluster (putative FPCs) were aggregated for transcription factor (ChEA) and pathway (Reactome) analysis. Results identified enriched proliferative signaling in FPCs. C) The expression of newly identified FPC markers (*Ass1*, *Sulf2*) and previously identified homeostatic (*Lgr5*) and injury-associated stem cell markers (*Clu, Hopx*) was analyzed across time in the *Ly6a*^{hi} and *Ly6a*^{lo} stem cell (*Gpx2+*) cluster. Note overall enrichment of *Ass1, Clu*, and *Sulf2* in the *Ly6a*^{hi} population, but specifically late upregulation of *Clu*. Total cell numbers in each cohort are written above the stacked bars. D) In situ hybridization (ISH) confirms upregulation of *Ass1* in injured crypts (asterisks). E) The heatmap shows genes upregulated in the time-resolved analysis of global epithelial gene expression through the stages of healing. Genes are clustered by their pattern of dynamic change. Overlapping cluster-specific markers are indicated in the side panel. F) Translation of dynamic gene-level expression changes to enriched MSigDB pathways. The results support differential representation of pathways in the epithelium at early vs. middle healing, consistent with the multi-phasic pattern of healing identified in imaging studies. G) The FPC markers in the "rise-middle" temporal pattern of panel E were used to derive a FPC conservative signature consisting of 20 genes. Pathway analysis revealed consistent upregulation of splicing-associated proteins and metabolic signaling (e.g., mTORC1, serine metabolism) across multiple databases. H) Validation of upregulated genes of the FPC conservative signature, derived from DSS injury, in the stem cells of *Il10*$^{-/-}$-mice. Significance test: paired t-test.
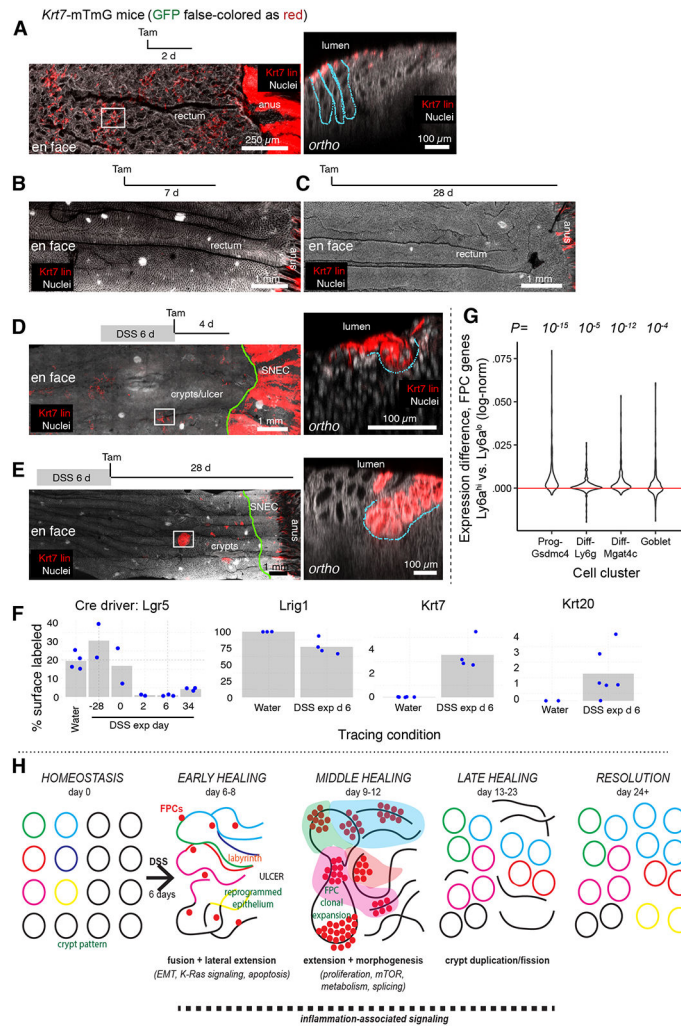
Figure 7: Long-term contribution of differentiated-cell lineages to repair.
Krt7-mTmG mice were injected with 2 mg tamoxifen to initiate lineage tracing (n 3
mice per condition). Shown are *en face* images and digitally reconstructed orthogonal
(ortho) zooms, with crypt-like structures outlined by the dotted blue line. The GFP signal
representing the *Krt7* lineage is false-colored as red to enhance visibility on the background
of brightly stained nuclei in lymphoid follicles. A) Short-term (2 d) tracing reveals labeled
cells at the luminal surface of crypts and in anal squamous tissue. B-C) Label within
the colonic epithelium is absent with longer-term tracing of 7 d (B) or 28 d (C) in
Krt7-mTmG mice. D) After DSS colitis, cells within regenerating crypts (white inset)
and the squamous neo-epithelium of colon (SNEC) are labeled. E) Long-term labeling
(28 d) after DSS colitis reveals foci (white inset) of fully labeled crypts. F) Surface
labeling quantification from lineage tracing after DSS colitis with different CreER driver
lines (see supplementary figures), categorized by day of tracing initiation. The results
demonstrate contributions of *Lgr5*-descendent, *Lrig1+* (lower crypt), *Krt7+* (upper crypt),
and *Krt20+* (upper crypt) cells. G) Violin plots show the aggregate difference in expression
of FPC genes (cf. Fig. 6A) between *Ly6a^{hi}* and *Ly6a^{lo}* cellular subpopulations for each
epithelial cell type. Significance test: Bonferroni-corrected paired t-test with alternate

hypothesis that differences in expression >0. H) Full diagram of crypt lineage intermixing and morphogenesis, FPC clonal expansion, and key signaling pathways underlying colonic epithelial wound healing in acute colitis.

KEY RESOURCES TABLE

REAGENT or RESOURCE	SOURCE	IDENTIFIER
Antibodies		
Rabbit anti-MGAT4C	Proteintech	RRID:AB_2143048
Mouse anti-GSDMC4	Aviva Systems Biology	ARP96264_P050
Rat anti-BrdU (BU1/75)	Abcam	RRID:AB_305426
Rat anti-Ki-67 (SolA15)	Thermo Fisher Scientific	RRID:AB_11219874
Chemicals, peptides, and recombinant proteins		
Dextran sulfate sodium 36-50kDa	MP Bio	0216011091
EdU	Cayman Chemical	20518
BrdU	Abcam	ab142567
Azoxymethane	Millipore Sigma	A5486
Tamoxifen	Millipore Sigma	T5648-1G
Liberase TM	Millipore Sigma	5401119001
DNase I	Millipore Sigma	D5025
RBC lysis solution	Biolegend	420301
Doxorubicin	MedChem Express	HY-15142
SB 525334	MedChem Express	HY-12043
Y-27632	MedChem Express	HY-10071
MHY1485	MedChem Express	HY-B0795
nifuroxazide	MedChem Express	HY-B1436
FDI-6	MedChem Express	HY-112721
rapamycin	MedChem Express	HY-10219
Intesticult Organoid Growth Medium (Mouse)	STEMCELL Technologies	06005
Matrigel, growth factor reduced	Corning	356231
Primocin	Invivogen	ant-pm-05
Critical commercial assays		
RNAScope 2.5 HD Assay – Brown	Biotechne / ACDBio	322300
ImmPACT DAB Substrate	Vector Labs	SK-4105
ImmPACT VIP Substrate	Vector Labs	SK-4605
ImmPRESS HRP anti-Rabbit IgG Polymer Kit	Vector Labs	MP-7801-15
ImmPRESS HRP anti-Mouse IgG Polymer Kit	Vector Labs	MP-7802-15
Chromium	10X Genomics	NA
EasySep Dead Cell Removal Kit	STEMCELL Technologies	17899
Deposited data		
Mouse single-cell RNA-Seq data	This paper	GSE193342
Data analysis scripts	This paper	DOI: 10.5281/zenodo.8201653
IBD single-cell RNA-Seq data	Smillie et al.[42]	SCP259
Experimental models: Genetically modified mice		

REAGENT or RESOURCE	SOURCE	IDENTIFIER
Rosa26::LSL-tdTomato (Ai14)	Jackson Laboratory[62]	RRID:IMSR_JAX:007914
Rosa26::-tdtTomato/-EGFP (mTmG)	Jackson Laboratory[63]	RRID:IMSR_JAX:007676
Rosa26::Brainbow2.1 (Confetti)	Jackson Laboratory[33]	RRID:IMSR_JAX:013731
Vil1::CreER	Jackson Laboratory[64]	RRID:IMSR_JAX:020282
Lgr5::EGFP-IRES-CreER	Jackson Laboratory[65]	RRID:IMSR_JAX:008875
Lrig1::CreER	Jackson Laboratory[44]	RRID:IMSR_JAX:018418
Krt7::CreER	Jiang et al.[45]	NA
Krt20::CreER	Jackson Laboratory[66]	RRID:IMSR_JAX:030600
Bl/6 (WT)	Jackson Laboratory	RRID:IMSR_JAX:000664
Il10–/–	Jackson Laboratory	RRID:IMSR_JAX:002251
Software and algorithms		
Cellranger v3.0.2	10X Genomics	https://support.10xgenomics.com/single-cell-gene-expression/software/pipelines/latest/what-is-cell-ranger
Monocle3	Cao et al.[54]	https://cole-trapnell-lab.github.io/monocle3/
Enrichr	Chen et al.[57]	https://maayanlab.cloud/Enrichr/
GSEA v4.0.0	Subramanian et al.[67]	https://www.gsea-msigdb.org/gsea/index.jsp
Fiji	Schindelin et al.[68]	https://fiji.sc/
Deep Mucosal Imaging	Liu et al.[29]	https://github.com/stalepig/deep-mucosal-imaging
Bowtie2 v2.3.5.1	Langmead and Salzberg[60]	https://github.com/BenLangmead/bowtie2
Bcftools v1.9	Li[61]	http://www.htslib.org/
Samtools v1.9	Li et al.[69]	http://www.htslib.org/
Other		
RNAScope probe – Mm-Gpx2	Biotechne / ACDBio	838451
RNAScope probe – Mm-Ass1	Biotechne / ACDBio	447991
RNAScope probe – Mm-Clu	Biotechne / ACDBio	427891
RNAScope probe – Mm-Sulf2	Biotechne / ACDBio	467901
RNAScope probe – Mm-Ly6a	Biotechne / ACDBio	427571